Coastal Engineering 186 (2023) 104391

Contents lists available at ScienceDirect

Coastal Engineering

journal homepage: www.elsevier.com/locate/coastaleng

Numerical modeling of tsunamis generated by granular landslides in OpenFOAM®: A Coulomb viscoplastic rheology

Alessandro Romano [a,b,*], Javier L. Lara [b], Gabriel Barajas [b], Íñigo J. Losada [b]

[a] Roma Tre University, Engineering Department, Via Vito Volterra 62, Rome 00146, Italy
[b] IHCantabria - Instituto de Hidráulica Ambiental de la Universidad de Cantabria, Calle Isabel Torres 15, Santander 39011, Spain

ARTICLE INFO

Keywords:
Granular landslides
Numerical modeling
Tsunamis
Water waves

ABSTRACT

Landslide-generated tsunamis are a relevant hazard. Their low frequency/high consequences character and the complex phenomena related to their generation, propagation and interaction with the shore make the proper modeling of these phenomena a crucial activity to mitigate the related risk. In this article, a new numerical method for modeling tsunamis generated by granular landslides in OpenFOAM® is presented. The approach consists in modeling the granular material by using a Coulomb viscoplastic rheology (non-Newtonian rheology) implemented in the standard solver *multiPhaseInterFoam*. The proposed approach is simple as it only depends on few physics-based parameters, thus implying less uncertainties than dense fluid models and more flexibility and computational efficiency than Euler–Euler approaches. This numerical framework is applied to reproduce three literature benchmark landslide-tsunami cases: two-dimensional (2D) submerged as well as 2D and three-dimensional (3D) subaerial. Comparing numerical and experimental results, a good agreement is found for granular material behavior, while an overall very good (excellent in some cases) agreement is found as far as fluid behavior and waves characteristics are concerned, testifying that the momentum transfer between granular and fluid phases is well reproduced by this simple rheological model. Qualitative descriptions of the numerical results, in terms of landslide behavior, wave generation characteristics, and velocity field during the generation/propagation process are provided. Moreover, quantitative comparisons between experimental and numerical results by comparing landslide evolution, free surface elevation time series, and runup time series are presented and discussed in the article.

1. Introduction

Landslide-generated tsunamis are a relevant source of hazard. As well known, landslide tsunamis are generally characterized by smaller length and time scales than those of tsunamis generated by earthquakes and, when a landslide occurs directly at the water body boundaries, the effects of the impulsive waves (e.g., runup, inundation, edge waves, radiated waves, Bellotti and Romano, 2017) can be magnified by the local geometry, especially for confined geometries (e.g., bays, reservoirs, lakes, and fjords, Heller and Ruffini, 2023).

Landslide tsunami risk is dominated by rare but, often, very destructive events causing numerous casualties and consistent socio-economic losses. It is worth citing the event which occurred in 1958 at Lituya Bay (Alaska, Fritz et al., 2009) that caused the largest wave runup recorded in modern times (524 m) killing 5 people, the Vajont Valley event (Italy, Panizzo et al., 2005) in 1963, that destroyed 4 villages causing the loss of nearly 2000 human lives and resulted in severe socio-economic consequences. Furthermore, it is worth mentioning the 1929 Grand Banks event (Canada, Zengaffinen et al., 2020) and the one of 1998 in Papua New Guinea (Synolakis et al., 2002), causing approximately 2200 fatalities, both triggered by large submarine mass failures, and, more recently, the tsunami which occurred in 2002 at Stromboli Island (Italy, Tinti et al., 2005) and the Anak Krakatoa event (Indonesia, Grilli et al., 2019) in 2018, when a volcano flank collapse triggered a tsunami that caused several hundreds of casualties.

The low frequency/high consequences character of tsunamis in general, and landslide-generated tsunamis in particular, induces considerable uncertainty into hazard assessment of such events. Furthermore, these are highly localized phenomena, both in space and time, and, unlike cyclones and storm surges, the lack (or the incompleteness) of historical records hinders in predicting the future level of hazard. Thus, the proper understanding and modeling of these phenomena is crucial, also for improving Tsunamis Early Warning Systems (TEWS) (Cecioni

* Corresponding author at: Roma Tre University, Engineering Department, Via Vito Volterra 62, Rome 00146, Italy.
E-mail address: alessandro.romano@uniroma3.it (A. Romano).

https://doi.org/10.1016/j.coastaleng.2023.104391
Received 19 May 2023; Received in revised form 30 August 2023; Accepted 4 September 2023
Available online 8 September 2023

et al., 2011; De Girolamo et al., 2014) and Probabilistic Tsunamis Hazard Assessment (PTHA) tools (Grilli et al., 2009; Løvholt and Harbitz, 2020).

Due to the complex physical phenomena involved in the tsunami generation, near-field and far-field wave propagation and interaction with the coast, landslide tsunamis are investigated by means of physical, numerical and analytical modeling. As far as physical model experiments are concerned, different approaches have been pursued in the last years, considering both rigid (Watts, 1998; Liu et al., 2005; Enet and Grilli, 2007; Di Risio et al., 2009a,b; Heller and Spinneken, 2013; Romano et al., 2013, 2016, 2017; Bellotti and Romano, 2017; Heller and Spinneken, 2015) and deformable/granular (Heller and Hager, 2010; Mohammed and Fritz, 2012; Viroulet et al., 2014; Lindstrøm, 2016; McFall and Fritz, 2016; Zitti et al., 2016; Grilli et al., 2017; Miller et al., 2017; Takabatake et al., 2022) landslides in 2D and 3D configurations.

Similarly, as far as numerical models are considered, several approaches are available, based on Eulerian and Lagrangian frameworks with three grid types (structured, unstructured, and meshless) used for modeling landslide tsunamis, employing either depth-averaged models, using Nonlinear Shallow Water or Boussinesq Equations, and Navier–Stokes models, considering both 2D and 3D configurations (e.g., Watts et al., 2003; Lynett and Liu, 2005; Liu et al., 2005; Løvholt et al., 2005; Bellotti et al., 2008; Cecioni et al., 2011; Yavari-Ramshe and Ataie-Ashtiani, 2016; Grilli et al., 2017; Whittaker et al., 2017; Si et al., 2018; Kim et al., 2019b; Ruffini et al., 2019; Grilli et al., 2019; Heidarzadeh et al., 2020).

Recently, significant efforts have been spent in developing modeling techniques of landslide tsunamis by using computational fluid dynamics (CFD) methods. In fact, these methods can be very useful to model in detail the complex phenomena that take place during the generation and near-field propagation/interaction with the coast phases. Similarly to physical model tests, in CFD numerical methods different approaches have been pursued to simulate landslide-generated tsunamis, modeling the landslide body as a rigid impermeable model (e.g., Montagna et al., 2011; Heller et al., 2016; Whittaker et al., 2017; Kim et al., 2019a; Chen et al., 2020; Romano et al., 2020) or as a deformable/granular material (Løvholt et al., 2005; Abadie et al., 2010; Ma et al., 2015; Shi et al., 2016; Kim et al., 2019b; Si et al., 2018; Clous and Abadie, 2019; Mulligan et al., 2020; Franci et al., 2020; Paris et al., 2021; Rauter et al., 2021, 2022; Lee and Huang, 2022; Guan and Shi, 2023), allowing also to successfully replicate/simulate complex case studies (La Palma, Canary Island, Abadie et al., 2012, 2019), Anak Krakatau (Indonesia, Grilli et al., 2019; Paris et al., 2020), and Lake Askja (Iceland, Rauter et al., 2022).

In the recent years, the open-source OpenFOAM® framework has become popular among the CFD tools due to its high level of accuracy, flexibility, and customizability. In fact, focusing on the numerical modeling of tsunamis generated by deformable/granular landslides, this framework has been recently used to successfully simulate these complex phenomena (e.g., Si et al., 2018; Rauter et al., 2021; Paris et al., 2021; Rauter et al., 2022). In order to simulate the behavior of granular materials in OpenFOAM®, roughly two families of approaches can be identified, namely: (I) dense fluid approaches and (II) Euler–Euler approaches. In the first methods, a single set of mass and momentum conservation equations is solved for both the granular and the fluid phase, and the granular material is modeled as a fluid characterized by its own density and viscosity (e.g., Paris et al., 2021; Rauter et al., 2021), also taking advantage of Newtonian and non-Newtonian (in which shear stress is not directly proportional to deformation rate) continuum rheologies originating from hydromechanics and soil mechanics. While, in the latter methods, different mass and momentum conservation equations are solved and coupled for both granular and fluid phases (e.g., Si et al., 2018; Rauter et al., 2022). Both approaches have advantages and disadvantages. On the one hand, dense fluid models are computationally efficient, nevertheless, to determine the viscosity value might be problematic, as clearly demonstrated by Paris et al. (2021). On the other hand, Euler–Euler approaches are more accurate, nevertheless, they are characterized by higher computational demand and potentially by higher uncertainty, related to the larger number of physical parameters and equations needed.

The modeling of granular material behavior in general, and the modeling of the interaction and momentum transfer between granular and fluid phases in particular, is still a challenging topic in research. In fact, depending on the flow configuration, granular material deformation may behave as an elastic, plastic, or viscous material, or the combination of them (Ancey, 2007; Domnik and Pudasaini, 2012). As pointed out by Ancey (2007), determining the rheological behavior of geophysical materials remains difficult because they encompass coarse, irregular particles over a very wide range of size. Consequently, the true nature of plastic behavior for geophysical flows is still vigorously debated. Several materials, including granular materials, may be modeled as viscoplastic fluids. These fluids (e.g., Bingham fluids) typically behave as single-phase fluids on the macroscopic scale and exhibit a viscous behavior after yielding.

In this article, a new numerical approach to model tsunamis generated by granular landslides in OpenFOAM® is presented. The numerical approach consists in modeling the granular material by using a Coulomb viscoplastic non-Newtonian rheological model (Domnik and Pudasaini, 2012; von Boetticher et al., 2016), which includes some basic features and observed phenomena in dense granular flows (Domnik and Pudasaini, 2012), implemented in the standard solver *multiPhaseInterFoam*. The advantage of this approach lies in its simplicity, flexibility and computational efficiency. In fact, it only depends on few physics-based parameters (e.g., internal friction angle and density), thus implying less uncertainties in determining the viscosity value than dense fluid models (Paris et al., 2021). Furthermore, it is more flexible and computationally efficient than Euler–Euler approaches, although the modeling of the landslide dynamics could be less accurate (Lee and Huang, 2022; Rauter et al., 2022), as some physical phenomena (e.g., mixing and permeation among phases) are not well reproduced and/or neglected. Nevertheless, the flexibility and computational efficiency favor the simulation of complex 3D cases, not addressed in previous studies using a similar numerical framework (Rauter et al., 2021; Paris et al., 2021), in which runup features and wave trapping are relevant aspects. This numerical framework is applied to reproduce three benchmark cases, aiming at exploring a wide range of initial/triggering conditions and configurations for landslide-generated tsunamis, identified by the tsunamis experts community (http://www1.udel.edu/kirby/landslide/problems.html Kirby et al., 2022), namely: a 2D submerged landslide case of Grilli et al. (2017), a 2D subaerial landslide case of Viroulet et al. (2014), and a 3D subaerial (accelerated) landslide case of Mohammed and Fritz (2012), respectively. Thus, the aim of the present article is to present the numerical approach and to test it under a wide range of geometrical configurations (2D and 3D) and landslide initial conditions (submerged, subaerial, and accelerated).

This article is structured as follows. After the introduction, the description of the numerical model framework (i.e., OpenFOAM®) and the rheological model used to simulate the granular landslides is provided. Then, a brief description of the experimental benchmark cases of landslide-generated tsunamis is given together with the numerical setup used to reproduce numerically those experiments. A results and discussion section follows. Finally, a concluding remarks section closes the article.

2. Numerical model

The numerical modeling of tsunamis generated by deformable landslides, described in this article, has been developed on the OpenFOAM® framework (Jasak, 1996). IHFOAM (Higuera et al., 2013a,b), based on *interFoam* of OpenFOAM®, includes wave boundary conditions for

coastal and offshore engineering applications and are used to solve the 3D Reynolds-Averaged Navier–Stokes equations (RANS) for two phase flows. RANS equations are solved coupled to the Volume of Fluid (VOF) equation. The base equations as well as a description of the proposed method are presented in this Section 2.

2.1. Governing equations

The RANS equations, used to model the flow, are based on the Reynolds decomposition, that identifies an average and a fluctuating component (i.e. velocity and pressure fields for incompressible models). These equations are represented by the mass and momentum conservation equations, coupled to the VOF equation as follows:

$$\frac{\partial u_i}{\partial x_i} = 0, \tag{1}$$

$$\frac{\partial \rho u_i}{\partial t} + u_j \frac{\partial \rho u_i}{\partial x_j} = -g_j x_j \frac{\partial \rho}{\partial x_i} - \frac{\partial p^*}{\partial x_i} - f_{\sigma i} - \frac{\partial}{\partial x_j}\mu_{\text{eff}}\left(\frac{\partial \rho u_i}{\partial x_j} + \frac{\partial \rho u_j}{\partial x_i}\right), \tag{2}$$

$$\frac{\partial \alpha}{\partial t} + \frac{\partial u_i \alpha}{\partial x_i} + \frac{\partial u_{ci}\alpha(1-\alpha)}{\partial x_i} = 0, \tag{3}$$

where subscript $i = 1, 2, 3$, as well as j, represent the three coordinate directions, obeying the Einstein summation convention, u_i (m/s) are the ensemble averaged components of the velocity, x_i (m) the Cartesian coordinates, g_j (m/s^2) the components of the gravitational acceleration, ρ (kg/m^3) the density of the fluid, p^* the ensemble averaged pressure in excess of hydrostatic, defined as $p^* = p - \rho g_j x_j$ (Pa), being p the total pressure, α (-) the volume fraction (VOF indicator function) which is assumed to be 1 for the water phase and 0 for the air phase, $f_{\sigma i}$ (N/m^3) the surface tension, defined as $f_{\sigma i} = \sigma\kappa\frac{\partial \alpha}{\partial x_i}$, where σ (N/m) is the surface tension constant and κ (1/m) the curvature (Brackbill et al., 1992). μ_{eff} (Pa · s) is the effective dynamic viscosity that is defined as $\mu_{\text{eff}} = \mu + \rho\nu_t$ and takes into account the dynamic molecular (μ) and the turbulent viscosity effects ($\rho\nu_t$); ν_t (m^2/s) is the eddy viscosity, which is provided by the turbulence closure model. Finally, the compression velocity u_{ci} (m/s) is calculated as $u_{ci} = \min[c_\alpha|u_i|, \max(|u_i|)]\frac{\frac{\partial \alpha}{\partial x_i}}{|\frac{\partial \alpha}{\partial x_i}|}$, where the compression coefficient c_α (-) is assumed to be 1 (Weller, 2008; Marschall et al., 2012).

Finally, it should be mentioned that the solver supports several turbulence models (e.g. two equation models, $k-\varepsilon$, $k-\omega$ and $k-\omega-SST$). In this study, the $k-\omega-SST$ (Shear Stress Transport) turbulence model, designed to yield the best behavior of the $k-\varepsilon$ and $k-\omega$ models, with the enhancement from Larsen and Fuhrman (2018) to deal with the overproduction of turbulence levels, has been used.

2.2. Non-Newtonian Coulomb viscoplastic rheology

To simulate the behavior of the granular material (i.e., the deformable landslide) and to simulate the interaction between landslides (both submerged and subaerial) and water bodies inducing the generation, propagation and interaction with the coast of lanslide-generated tsunamis, a Coulomb viscoplastic non-Newtonian rheological model (Domnik and Pudasaini, 2012) has been implemented in the OpenFOAM® framework in the standard solver *multiPhaseInterFoam*. It is important to highlight that this rheology has been originally implemented and validated in OpenFOAM® by von Boetticher et al. (2016) in the solver *interMixingFoam* to study debris flows occurring in air (i.e., no interaction between debris flow and clear water bodies).

Here a brief description, based on the work of von Boetticher et al. (2016), of the rheology model, is provided. The reader is referred to Domnik and Pudasaini (2012) and von Boetticher et al. (2016) for further details related to theoretical aspects.

As stated by Domnik and Pudasaini (2012), flows of granular material could be modeled as viscoplastic fluids, where the granular Cauchy stress tensor $\mathbf{T}_s$ can be written as

$$\mathbf{T}_s = -p\mathbf{I} + 2\mu_s\mathbf{D}, \tag{4}$$

where $p\mathbf{I}$ is the pressure times the identity matrix and μ_s is the corresponding dynamic viscosity, which was modeled by Domnik and Pudasaini (2012) as

$$\mu_s = \mu_{min} + \frac{\tau_{0s}}{\|\mathbf{D}\|}\left(1 - \exp^{-m_y\|\mathbf{D}\|}\right), \tag{5}$$

where μ_{min} is a minimal dynamic viscosity, τ_{0s} is a yield stress, and $\|\mathbf{D}\|$ is the norm of the strain-rate tensor defined by Domnik and Pudasaini (2012) as

$$\|\mathbf{D}\| = \sqrt{2\text{tr}(\mathbf{D}^2)}, \tag{6}$$

while m_y is a numerical parameter with units of seconds. Consistently with von Boetticher et al. (2016), m_y is kept constant in this article. Domnik et al. (2013) derived the yield stress as a pressure-dependent Coulomb friction, $p\sin(\delta)$, being δ the internal friction angle of the granular material. Therefore, Eq. (5) can be written as

$$\mu_s = \mu_{min} + \frac{p\sin(\delta)}{\|\mathbf{D}\|}\left(1 - \exp^{-m_y\|\mathbf{D}\|}\right). \tag{7}$$

Therefore, this Coulomb viscoplastic rheology model is used to simulate the granular material (i.e., the landslide). As stated by von Boetticher et al. (2016), the pressure- and shear-dependent viscosity is calculated in every cell with the corresponding local pressure p and strain-rate tensor $\mathbf{D}$ derived from the phase-averaged flow field. Thus, if the granular phase is considered, $\mu_{\text{eff}} = \mu_s$ in Eq. (2).

In this work, this rheological model has been added to the standard OpenFOAM viscosity library and linked to the standard OpenFOAM solver *multiPhaseInterFoam*, to simulate an immiscible sliding granular flow interaction with water, with an additional unmixed phase representing the air.

3. Description of the benchmark experiments and numerical setup

To test the capability of the numerical approach to reproduce tsunamis induced by granular (i.e., deformable) landslides a set of three experimental benchmark cases from the literature has been numerically reproduced. They have been selected with the aim of exploring a wide range of initial/triggering conditions and configurations for landslide-generated tsunamis. In fact, different initial landslide positions, spanning from submerged to subaerial landslides, and velocities, spanning from resting to accelerated landslides, have been chosen thus investigating and stressing the capability of the numerical model to reproduce different landslide conditions.

With this in mind, the three selected benchmarck cases are: (I) a 2D case of waves generated by submerged deformable landslides of Grilli et al. (2017); (II) a 2D case of waves generated by subaerial deformable landslides of Viroulet et al. (2014); (III) a 3D case of waves generated by a subaerial (accelerated) deformable landslide of Mohammed and Fritz (2012).

In the following a brief description of each experimental benchmark is provided, together with the description of the numerical setup/implementation. The readers are referred to the mentioned works for further details on the experimental conditions.

3.1. Grilli et al. (2017) : 2D submerged landslide

These laboratory experiments of tsunamis generated by underwater deformable landslides have been performed at the Ecole Centrale de Marseille (IRPHE, Marseille, France). The experimental setup was made up of a wave flume of length $l = 6.27$ m and width $w = 0.25$ m and a slope (slope angle $\theta = 35°$) was placed at one edge of the flume. The granular landslides are modeled by a volume of glass beads (density $\rho_b = 2500$ kg/m^3). In each experiment, a mass of beads was submerged in fresh water (density $\rho_w = 1000$ kg/m^3), in a reservoir of triangular shape located on the slope, fronted by a sluice gate.

The experiments consisted in instantaneously withdrawing the gate, thus the beads were released along the slope, generating the impulsive

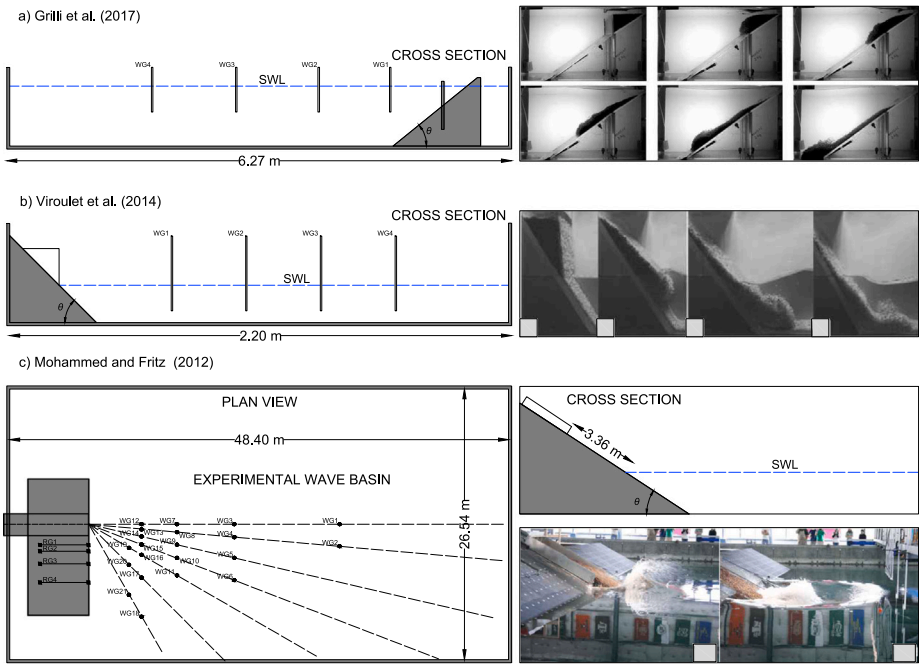

Fig. 1. Sketches and pictures of the experimental benchmarks. Upper panels: submerged 2D landslide case (Grilli et al., 2017). Middle panels: subaerial 2D landslide case (Viroulet et al., 2014). Lower panels: subaerial 3D landslide case (Mohammed and Fritz, 2012). Note: pictures are adapted from Grilli et al. (2017), Viroulet et al. (2014), and Mohammed and Fritz (2012), respectively.

waves. During the experiments the water depth (h = 0.320–0.370 m), beads diameter (d_b = 4 and 10 mm) and dry mass (M_b = 1.5–2.5 kg) have been varied. Each experiment was recorded using a high-speed video camera placed on the side of the tank to trak the underwater motion of the beads. Furthermore, time series of free surface elevations were measured at four wave gages WG1–WG4 placed along the flume. Pictures of the experiments are shown in the panel a) of Fig. 1.

In this work, test 17 (described in http://www1.udel.edu/kirby/landslide/problems.html), has been numerically reproduced (h = 0.33 m, d_b = 4 mm, M_b = 2.0 kg). A 2D numerical wave flume with a length l = 6.27 m, a width w = 0.02 m and a total height h_f = 0.50 m has been created. A general mesh with a spatial resolution of Δx, Δz = 0.005 m has been adopted in the numerical domain, while an extra refinement with spatial resolution Δx, Δz = 0.0025 m has been applied around the free surface, along the slope and at the toe of the slope (i.e., runout region). The numerical wave flume, and an example of the computational mesh, are reported in the panel a) of Fig. 2. As for the rheological model of the granular material, the following parameters values have been used: bulk density ρ_b = 1951 kg/m^3, internal friction angle δ = 34.0°, and minimal dynamic viscosity μ_{min} = 1e − 6 m^2/s. Impermeable surface boundary conditions have been applied at the slope surface, at the bottom and at the wall of the wave flume.

The simulations were performed using a computer desktop with the following characteristics: Intel® Core™ i7-7700K CPU 4.20 GHz CPU unit, 32 GB RAM. To simulate 5 s using 1 processor (the mesh has 0.19M cells), a total time of approximately 10 h were needed.

3.2. Viroulet et al. (2014) : 2D subaerial landslide

These laboratory experiments of tsunami generated by subaerial deformable landslides have been performed at the Ecole Centrale de Marseille (IRPHE, Marseille, France). The experimental setup is made up of a wave flume of length l = 2.20 m and width w = 0.20 m and a slope (θ = 35°–60°) was placed at one edge of the flume. The granular landslides were modeled with a volume of glass beads (density ρ_b = 2500 kg/m^3) initially contained in a triangular cavity, placed above the still water level (h = 0.148 m) and fronted by a sluice gate. In each experiment, a mass of beads was submerged in fresh water (ρ_w = 1000 kg/m^3), in a reservoir of triangular shape located on the slope. The experiments consisted in instantaneously withdrawing the gate, thus the beads were released along the slope, generating the impulsive waves. Time series of free surface elevations were measured at four wave gages WG1–WG4 placed along the flume. Pictures of the experiments are shown in the panel b) of Fig. 1.

In this work, the test with θ = 45°, h = 0.148 m and d_b = 1.5 mm, described in http://www1.udel.edu/kirby/landslide/problems.html, has been numerically reproduced. A 2D numerical wave flume with a length l = 2.20 m, a width w = 0.02 m and a total height h_f = 0.45 m has been created. A general mesh with a spatial resolution of Δx, Δz = 0.005 m has been adopted in the numerical domain, while an extra refinement with spatial resolution Δx, Δz = 0.0025 m has been applied around the free surface, along the slope and at the toe of the slope (i.e., runout region). The numerical wave flume and an example of the computational mesh are reported in panel b) of Fig. 2. As for the rheological model of the granular material, the following parameters values have been used: ρ_b = 1585 kg/m^3, δ = 23.0° and μ_{min} = 1e − 6 m^2/s. Impermeable surface boundary conditions have been applied at the slope surface, at the bottom and at the wall of the wave flume.

The simulations were performed using a computer desktop with the following characteristics: Intel® Core™ i7-7700K CPU 4.20 GHz CPU unit, 32 GB RAM. To simulate 3 s using 1 processor (the mesh has 0.1M cells), a total time of approximately 3.5 h were needed.

3.3. Mohammed and Fritz (2012) : 3D subaerial landslide

These laboratory experiments of tsunami generated by subaerial deformable landslides have been performed in the tsunami wave basin (TWB) of the Network for Earthquake Engineering Simulation (NEES) at Oregon State University (Corvallis, Oregon, USA). The experimental setup was made up of a wave basin of length l = 48.80 m and width w = 26.50 m, with varying still water depths. A hillslope (θ = 27.1°) was placed at the left hand side of the basin. A 9.3 m long steel plate was used as sliding surface. The granular landslides were modeled by a volume of naturally rounded river gravel (particle size in the range

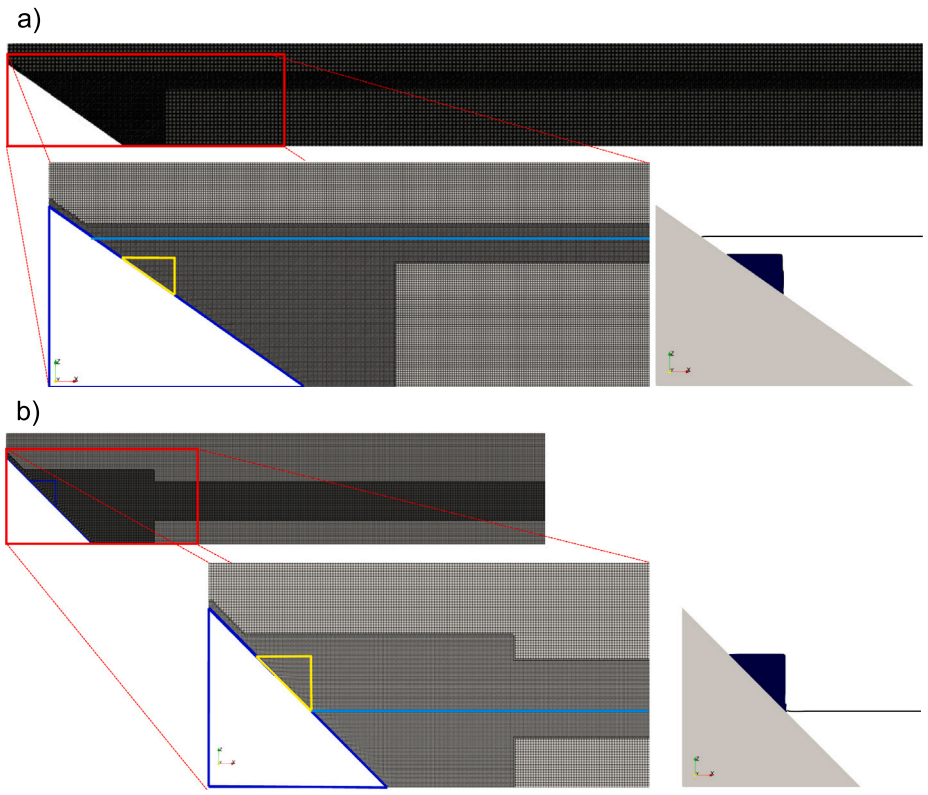

Fig. 2. Numerical setups, with zoom on the extra mesh refinement zones and initial positions of the landslides, used for the submerged 2D landslide case of Grilli et al. (2017) (panel a)) and for the subaerial 2D landslide case of Viroulet et al. (2014) (panel b)).

d_g = 6.35–19.05 mm, d_{50} = 13.7 mm and ρ_b = 2600 kg/m^3) initially contained into a box (2.1 m × 1.2 m × 0.3 m), placed on the sliding surface, that can be accelerated by a pneumatic pistons system.

The experiments consisted in accelerating the box containing the landslide, thus the slide velocity corresponding to the box velocity. The landslide was released as the box reaches the maximum velocity. Then, the deformable granular landslide collapsed down the hillslope while the box was decelerated and slid down simulating a gravity driven granular landslide. During the experiments, the water depth (h = 0.3, 0.6, 0.9 and 1.2 m) and pressure in the pneumatic pistons (P = 145, 116, 87 and 58 psi), corresponding to different landslide velocities, have been varied. Pictures of the experiments are shown in the panel c) of Fig. 1.

In this work, the test with h = 0.6 m and P = 58 psi, described in http://www1.udel.edu/kirby/landslide/problems.html, has been numerically reproduced. A 3D numerical wave tank with a length l = 30.00 m, a width w = 13.27 m and a total height h_f = 3.50 m has been created. A general mesh with a spatial resolution of Δx, Δy, Δz = 0.07 m has been adopted in the numerical domain, while an extra refinement with spatial resolution Δx, Δy, Δz = 0.0175 m has been applied around the free surface, along the slope (only around the landslide path) and at the toe of the slope (i.e., runout region). The numerical wave tank and an example of the computational mesh are reported in the panels a) and b) of Fig. 3. For the rheological model of the granular material ρ_b = 1760 kg/m^3, δ = 41.0°, and μ_{min} = 1e − 6 m^2/s have been used.

In contrast to the 2D tests, both the length and width of the numerical wave tank are smaller than those of the experimental one in order to save computational time. As for the length, a shorter value has been used to save computational time. In fact, since the focus of a CFD approach is on the near-field, it is not useful to model the whole length of the wave tank. Therefore, to avoid that spurious reflected waves contaminate the wave field, an absorbing boundary contidion (see Higuera et al., 2013a) has been applied at the east boundary of the numerical domain to allow the wave freely exiting from the domain along the x direction. As for the width, a symmetry plane, parallel to the centerline of the box containing the granular material, has been applied (see panel b) of Fig. 3). On the other boundaries of the numerical domain (i.e., slope surface, bottom and walls of the wave tank) impermeable surface boundary conditions have been applied.

Another difference, if compared with the physical model experiments, is related to the landslide initial or release conditions. In fact, as previously described, the experimental granular material is initially contained into a box, which is accelerated up to a certain velocity and then released. On the other hand, in the numerical simulations the acceleration phase of numerical granular material has not been modeled. Instead, the numerical simulations start at the same time instant at which the release of the experimental landslide occurs. Thus, in the numerical simulations, the granular material is released at an abscissa X_s^* (measured along the slope), having an initial velocity v_f^* which are identical to the ones of the experimental box, considered at the release time instant (see panels c) and d) of Fig. 3). Moreover, the initial landslide shape of the numerical landslisde is the same as of the box, while in the physical model experiments the acceleration phase could have slightly modified the initial shape of the granular material. Obviously, these differences in the initial conditions could have an influence in the numerical results, as discussed in detail in Section 4.

The simulations were performed using a HPC supercomputing cluster with 1276 cores, 29,53 TFlops, 5TB RAM and 130TB Storage 29.53 Tflops, 80 Compute nodes iDataPlex dx360 M4 Server (64 GB RAM, 2 * Intel® Xeon® CPU E5-2670 @ 2.60 GHz, IB FDR). Runs have been parallelized using 128 processor units (the mesh has 28.9M cells). To simulate 10 s, a total of approximately 9 days were needed.

3.4. Mesh optimization

For each benchmark case, a convergence analysis of the computational mesh has been carried out to tune the optimum value of the

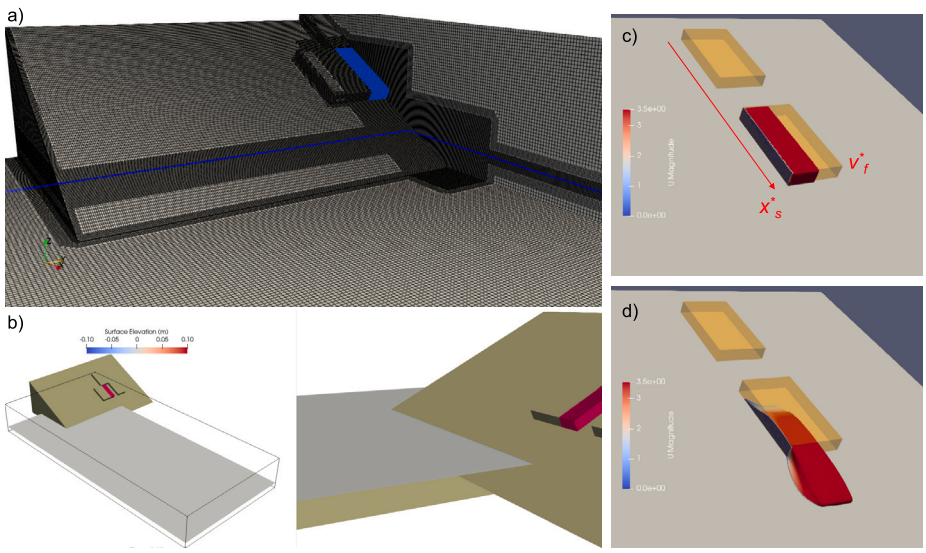

Fig. 3. Numerical setup, with zoom on the extra mesh refinement zones (panel a)) and initial position (panel b) and velocity (panels c), d)) of the landslide, used for the subaerial 3D landslide case of Mohammed and Fritz (2012).

Table 1
Mesh convergence analysis results for the three benchmarks. Note: $NMSE_{cWG}$ is calculated at the closest WG: WG1 for Grilli et al. (2017), WG1 for Viroulet et al. (2014) and WG12 for Mohammed and Fritz (2012), respectively. Values in brackets (·) are calculated neglecting the trailing waves.

	Mesh Name	$\Delta x, \Delta y, \Delta z$ General (m)	$\Delta x, \Delta y, \Delta z$ Refinement (m)	Number of cells	$NMSE_{cWG}$
Grilli et al. (2017)	M1	0.0063	0.0032	0.12 M	0.334 (0.103)
	M2	0.0050	0.0025	0.19 M	0.301 (0.075)
	M3	0.0038	0.0019	0.34 M	0.272 (0.051)
Viroulet et al. (2014)	M1	0.0063	0.0032	0.05 M	0.121
	M2	0.0050	0.0025	0.08 M	0.089
	M3	0.0038	0.0019	0.14 M	0.069
Mohammed and Fritz (2012)	M1	0.0900	0.0225	15.1 M	0.15
	M2	0.0700	0.0175	28.7 M	0.097
	M3	0.0500	0.0125	45.3 M	0.091

mesh size to be used for the simulations. To this end, three meshes (M1, M2 and M3) with increasing spatial resolution have been tested for each benchmark (see Table 1). In order to select the mesh to be used, the quantitative parameter $NMSE_{cWG}$ (Normalized Mean Squared Error between numerical and experimental signals, evaluated at the closest wave gauge to the landslide initial position) has been calculated. For each benchmark, the mesh M2 has been selected to be used for the following simulations, as it guarantees the best trade-off between accuracy and computational efficiency (particularly important for the 3D case).

4. Results and discussion

In this section, numerical results are analyzed, compared with the experimental ones and in-depth discussed. Firstly, a qualitative description of the numerical results, aiming at describing the physical process of the tsunami generation induced by the granular material, is given. Landslide behavior, waves characteristics, velocity field and free surface elevation pattern during the generation/propagation process are qualitatively presented and discussed for the three benchmark cases. Secondly, a quantitative comparison between experimental and numerical results, including a sensitivity analysis on the input parameters, is provided. The comparison is performed looking at three characteristics, namely: (I) landslide evolution, (II) free surface elevation time series, and (III) runup time series (for the 3D case only).

Fig. 4 shows six selected snapshots (t = 0.15, 0.21, 0.31, 0.41, 0.51, 0.71 s from panel a) to f), respectively) that depict the evolution in time of the interaction between the granular landslide and the water body for the submerged 2D case (Grilli et al., 2017). The velocity magnitude pattern, both for landslide and water, is represented in each panel by using color maps and streamlines, respectively. Furthermore, thin black lines identify the shape of the free surface elevations, while the gray filled areas represent the slope. Fig. 4 shows that the model is able to provide, at least from a qualitative point of view, a good reproduction of the physics. After the landslide starts to deform, sliding along the slope, a wave trough is generated above the initial position of the landslide. Then, while the landslide slides down, a wave crest is generated by the piston-like mechanisms and a rundown can be seen on the shore. The waves propagate away from the generation area, nevertheless, it appears, after the first time instants, that the granular material tends to be quite viscous and the sliding along the slope is slowed down, although this aspect is not evident from these snapshots. This is further discussed later.

A similar process is presented in Fig. 5, where six selected snapshots (t = 0.11, 0.19, 0.29, 0.39, 0.49, 2.50 s from panel a) to f), respectively) show the evolution in time of the interaction between the granular landslide and the water body for the subaerial 2D case (Viroulet et al., 2014). In this figure, the same nomenclature as for Fig. 4 is used. After the landslide triggering, the granular material starts to deform, sliding along the slope, hits the water surface and enters the water, generating a wave crest, following the typical piston-like mechanism. Then, the generated waves propagate away from the generation are and the landslide reaches the bottom of the flume, arresting its motion.

Figs. 6 and 7 refer to the numerical results of the subaerial 3D case (Mohammed and Fritz, 2012). Fig. 6 is divided into two parts. The

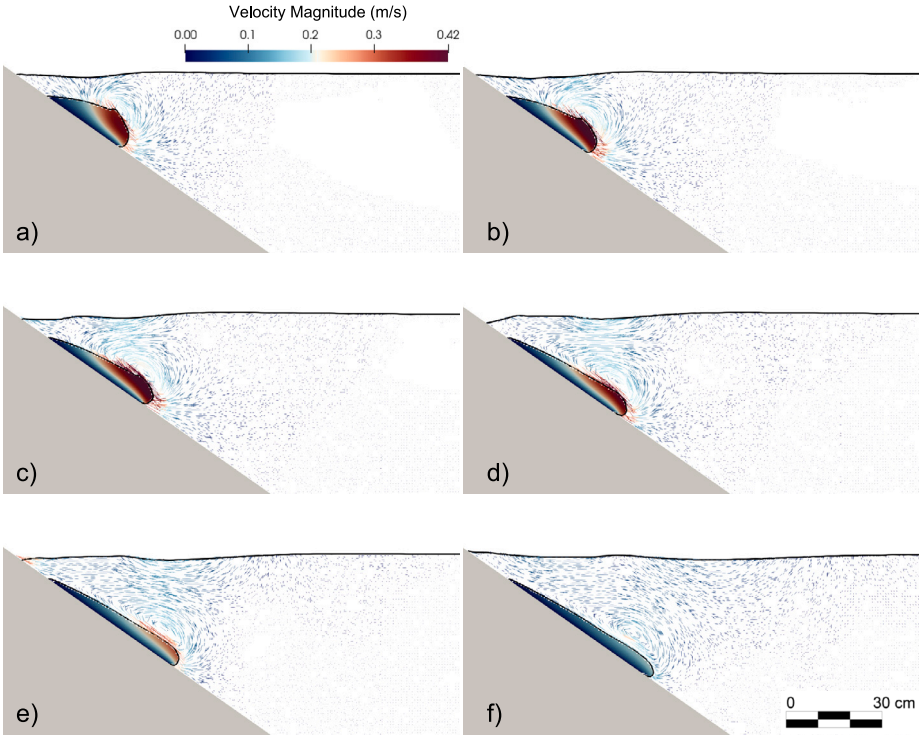

Fig. 4. Snapshots of the evolution in time (t = 0.15, 0.21, 0.31, 0.41, 0.51, 0.71 s from panel a) to f), respectively) of the interaction between the granular landslide and the water body for the submerged 2D case (Grilli et al., 2017). Note: the velocity magnitude pattern, both for landslide and water, is represented by using color maps and streamlines, respectively. The thin black lines identify the free surface elevations, while the gray filled areas represent the slope.

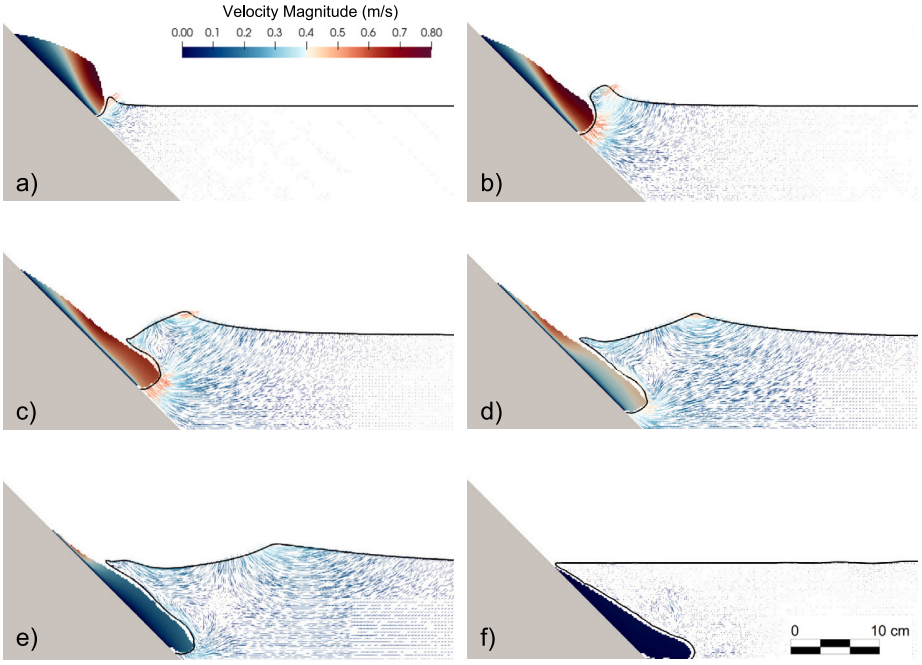

Fig. 5. Snapshots of the evolution in time (t = 0.11, 0.19, 0.29, 0.39, 0.49, 2.50 s from panel a) to f), respectively) of the interaction between the granular landslide and the water body for the subaerial 2D case (Viroulet et al., 2014). Note: the velocity magnitude pattern, both for landslide and water, is represented by using color maps and streamlines, respectively. The thin black lines identify the free surface elevations, while the gray filled areas represent the slope.

first and second columns show eight selected snapshots (t = 0.50, 1.00, 1.50, 2.00, 2.50, 3.00, 5.50, 12.23 s from panel a_1) to h_1), respectively) that depict the evolution in time of the interaction between the granular landslide and the water body along a cross section placed in the centerline of the landslide (i.e., on the numerical symmetry plane). The velocity magnitude pattern, both for landslide and water, is represented by using color maps. The third and fourth columns of Fig. 6 show the evolution in time of the interaction between the granular landslide (velocity magnitude pattern and evolution in space) and the water body at the same selected time instants previously reported (from panel a_2) to h_2), respectively) from a different perspective, showing also the free surface elevation pattern (gray scale).

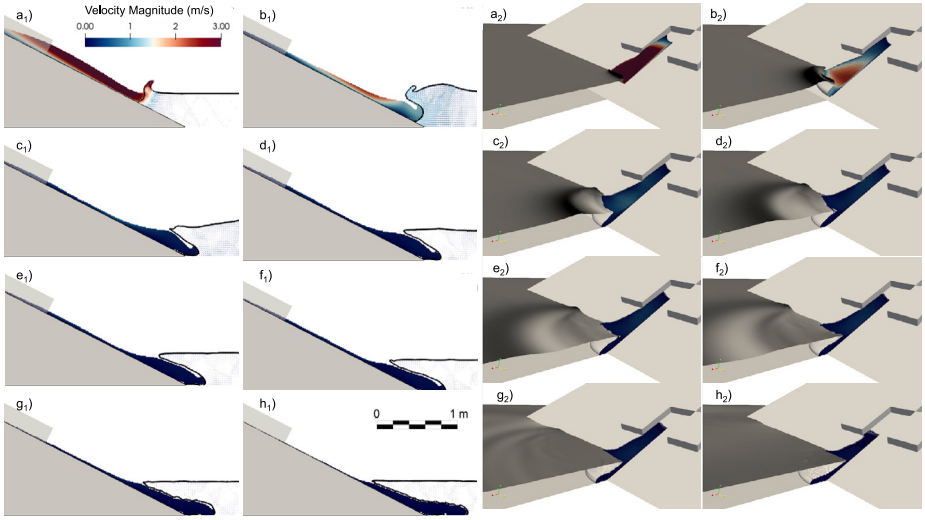

Fig. 6. Snapshots of the evolution in time (t = 0.50, 1.00, 1.50, 2.00, 2.50, 3.00, 5.50, 12.23 s) of the interaction between the granular landslide and the water body for the subaerial 3D case (Mohammed and Fritz, 2012) from different perspectives. Note: the velocity magnitude pattern, both for landslide and water, is represented by using color maps.

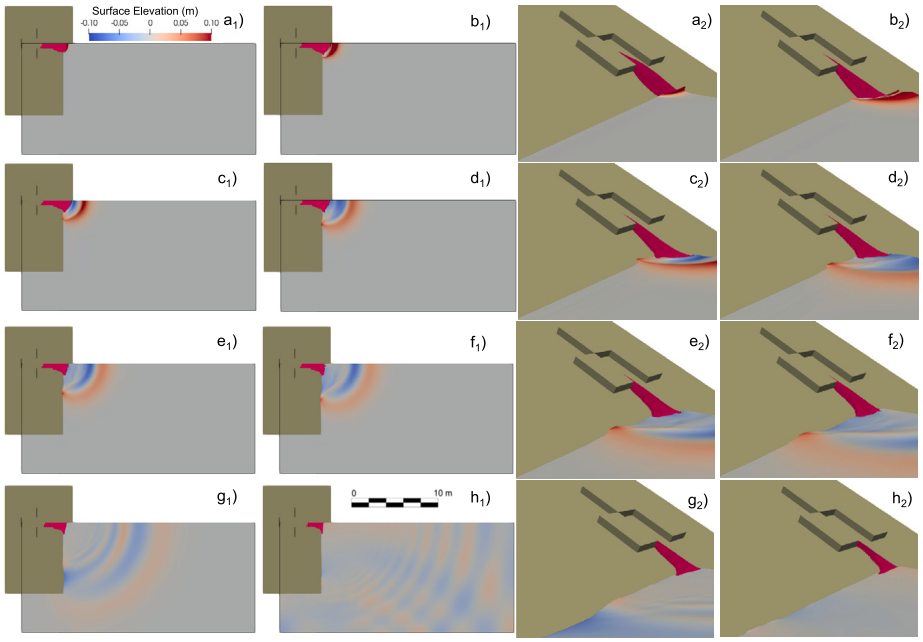

Fig. 7. Snapshots of the evolution in time (t = 0.50, 1.00, 1.50, 2.00, 2.50, 3.00, 5.50, 12.23 s) of the interaction between the granular landslide and the water body for the subaerial 3D case (Mohammed and Fritz, 2012) from different perspectives. Note: the free surface elevation pattern is represented by using color maps.

Based on Fig. 6 it is interesting to interpret the behavior of the model in reproducing the complex physical phenomena related to landslide-tsunamis generation physics. The landslide material sliding along the slope, hits the water surface and enters the water, generating a wave crest, following the typical piston-like mechanism. Then, the generated waves propagate away from the generation are and the landslide reaches the bottom of the flume, arresting its motion. Obviously, since this is a 3D case the landslide suffers also a lateral expansion and deformation.

Fig. 7 is, consistently, divided into two parts. The first and second columns show eight selected snapshots (t = 0.50, 1.00, 1.50, 2.00, 2.50, 3.00, 5.50, 12.23 s from panel a_1) to h_1), respectively) that depict a plan view of the evolution in time of the free surface elevation pattern (color scale), while the third and fourth columns (from panel a_2) to h_2), respectively) show, from a different perspective, the detail of the runup pattern close to the landslide impact area and along the shoreline. Fig. 7 confirms, from another point of view, the same physical considerations discussed in Fig. 6. It is worth noticing that this perspective magnifies the view of the runup pattern, typically dominated by the edge waves activity (Bellotti and Romano, 2017).

4.1. Landslide evolution

4.1.1. 2D Submerged landslide

Fig. 8 presents the comparison between the experimental and numerical landslide evolution along the slope (i.e., in space) at six selected time instants (t = 0.00, 0.02, 0.17, 0.32, 0.47, 0.62 s). In the figure, thin dashed blue lines refer to the undisturbed still water level, thick red lines refer to the numerical landslide evolution and black lines with dot markers refer to the experimental landslide evolution.

Fig. 8 shows that in the first time instants after the landslide release, the numerical and experimental results present a good agreement, both in shape and in timing. In fact, the numerical landslide front and

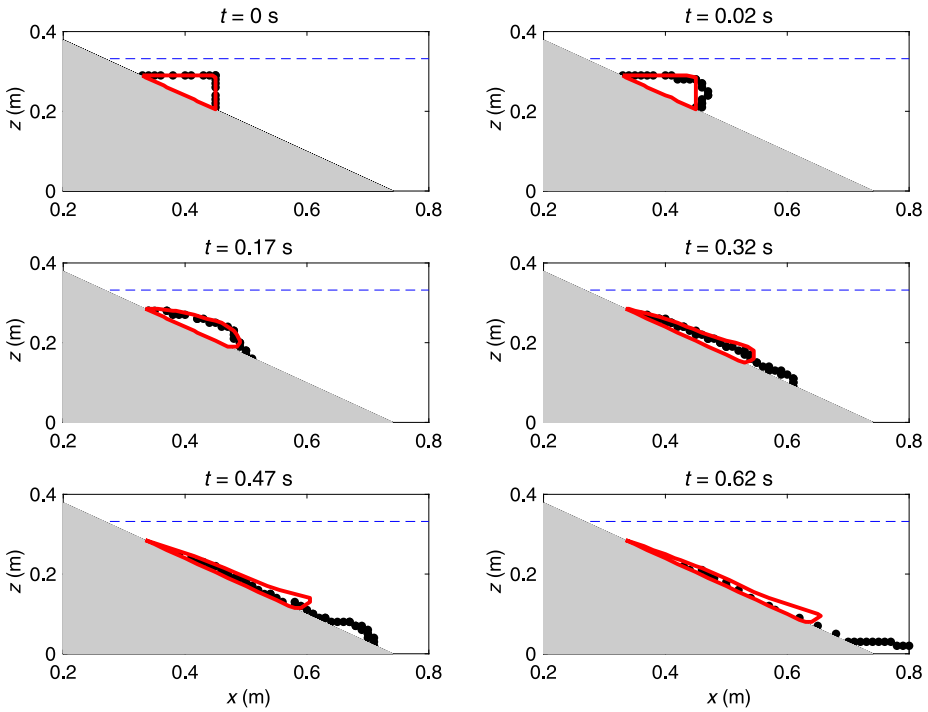

Fig. 8. Comparison between the experimental and numerical landslide evolution along the slope at six selected time instants (t = 0.00, 0.02, 0.17, 0.32, 0.47, 0.62 s) for the 2D submerged case of Grilli et al. (2017). Note: thin dashed blue lines refer to the undisturbed still water levels, thick red lines refer to the numerical landslide evolution and black lines with dot markers refer to the experimental landslide evolution.

thickness well resemble the experimental data. Nevertheless, starting from t = 0.32 s, the numerical results differ from the experimental results. It appears that the numerical landslide is slower than the experimental one, as reported also in previous works dealing with similar modeling approaches (e.g., Clous and Abadie, 2019; Paris et al., 2021). Therefore, for increasing time the difference between experimental and numerical landslide increases, resulting a very different runout pattern. Although the landslide evolution in the last part of its pattern is not well reproduced, this aspect will not necessarily reflect in a poor reproduction of the impulsive waves. In fact, it is well documented in the scientific literature that for submerged landslides most of the energy transfer between landslide and waves takes place at the very beginning of the landslide motion (Grilli et al., 2009; Clous and Abadie, 2019; Romano et al., 2020). This aspect is better discussed in the next sections, when numerical and experimental free surface elevation time series are compared.

4.1.2. 2D subaerial landslide

Fig. 9 presents the comparison between the experimental and numerical landslide evolution along the slope (i.e., in space) at six selected time instants (t = 0.00, 0.10, 0.20, 0.30, 0.40, 0.50 s). In the figure, thin dashed blue lines refer to the undisturbed still water levels, thick red lines refer to the numerical landslide evolution and black lines with dot markers refer to the experimental landslide evolution.

Fig. 9 shows that an overall very good agreement between experimental and numerical results can be seen for every time instant, both in shape and in timing. In fact, the numerical landslide front evolution is very similar, in time, to the experimental one throughout the whole process, while the numerical landslide shape slightly differ from the experimental one when the landslide approaches the flume bottom. Indeed, it can be noticed the lack of humps in the numerical landslide. This aspect is reasonable considering the numerical approach is based on a multiphase approach, in which mixing and permeation among phases are not properly modeled.

4.1.3. 3D subaerial landslide

Fig. 10 presents the comparison between experimental (empty black dots) and numerical (full red diamonds) landslide front velocity measured along the abscissa X_s, which is parallel to the slope. The first group of black markers (X_s < 1.0 m) refers to the acceleration phase of the box; so, no comparison is performed for this phase, which has not been reproduced numerically. Indeed, the comparison between experimental and numerical results starts after the box opening, i.e., when the landslide is released and starts sliding along the slope. In this phase, the numerical landslide front velocity is, at the very beginning, larger than the experimental one. This overestimation is probably a model effect due to discrepancies in the initial conditions. In fact, the numerical landslide is released having the initial shape and velocity of the box at the release time instant, while in the physical model experiments the acceleration phase could have slightly modified the initial shape of the granular material. Thus, it is possible that box-shape of the numerical granular material is not consistent with its velocity, causing this discrepancy. Note that a similar effect is noticed also looking at the landslide thickness, as discussed later. After the first time instants, numerical and experimental landslide front velocities are very similar up to the impact with the water surface.

Furthermore, the landslide thickness is analyzed. Fig. 11 shows the comparison between experimental (black lines) and numerical (red lines) landslide thickness ζ along the abscissa X_s after the landslide release (i.e., box opening). Each panel is a snapshot referring to a different time instant t^*, being t^* = 0 s the time instant at which the landslide hits the water surface, accordingly to the experimental results of Mohammed and Fritz (2012). Confirming what is shown in Fig. 10, during the initial phase after the landslide release the numerical landslide front appears to be faster than the experimental one. It is worth to remind that the phenomenon at hand is extremely fast as the box is accelerated; in fact, the granular material takes approximately 0.4 s to reach the water surface. Therefore, slight differences in the initial conditions may affect significantly the timing of the landslide front. Nevertheless, the landslide thickness is always comparable between experimental and numerical results. Thus, the reproduction of the landslide evolution along the slope is overall satisfactory.

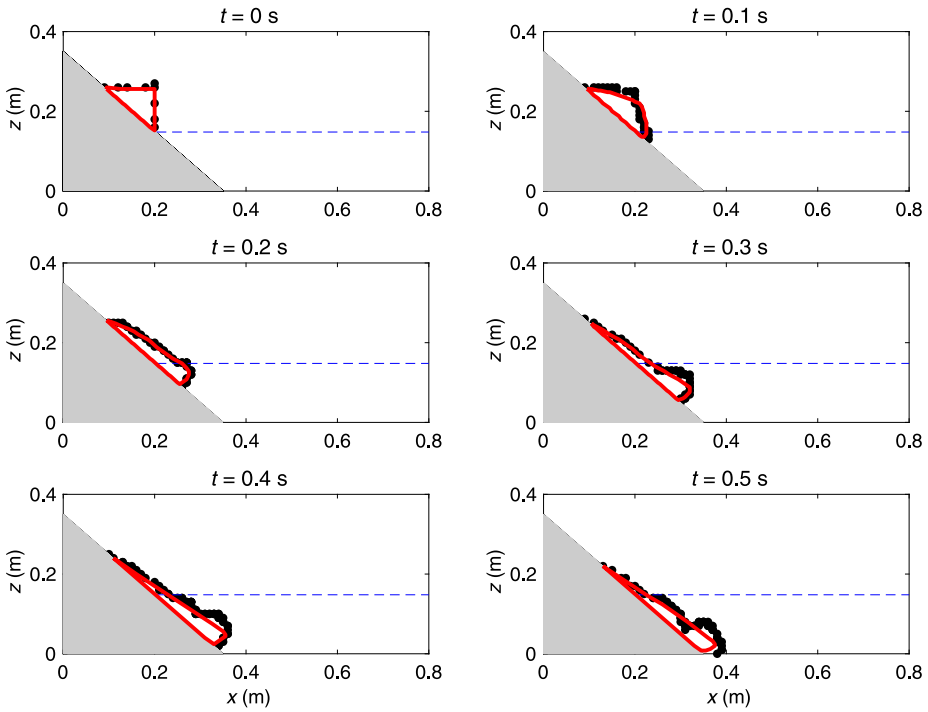

Fig. 9. Comparison between the experimental and numerical landslide evolution along the slope at six selected time instants (t = 0.00, 0.10, 0.20, 0.30, 0.40, 0.50 s) for the 2D subaerial case of Viroulet et al. (2014). Note: thin dashed blue lines refer to the undisturbed still water levels, thick red lines refer to the numerical landslide evolution and black lines with dot markers refer to the experimental landslide evolution.

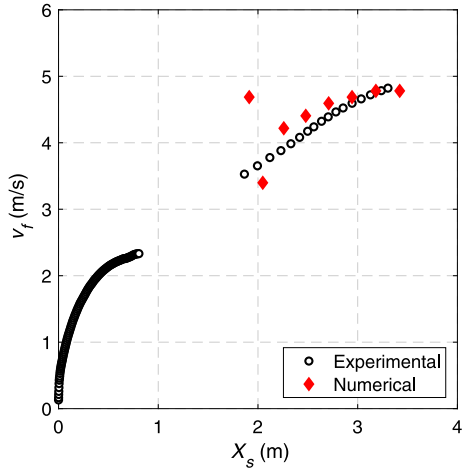

Fig. 10. Comparison between experimental (empty black dots) and numerical (full red diamonds) landslide front velocity measured along the abscissa X_s for the 3D subaerial case of Mohammed and Fritz (2012). Note: the first group of black markers (X_s < 1.0 m) refer to the acceleration phase of the box.

Table 2
Parameter values for the quantitative comparison between numerical and experimental results of the 2D submerged case of Grilli et al. (2017): $\Delta\eta_c^{max}$, $\Delta\eta_t^{min}$ and NMSE. Note: the values refer to the four wave gauges presented in Fig. 12. Values in brackets (·) are calculated neglecting the trailing waves.

Gauge name	$\Delta\eta_c^{max}$	$\Delta\eta_t^{min}$	NMSE
WG1	0.043	0.029	0.301 (0.075)
WG2	0.233	0.045	0.138 (0.048)
WG3	0.309	0.027	0.047
WG4	0.147	0.023	0.150

4.2. Free surface elevation

4.2.1. 2D Submerged landslide

Fig. 12 presents the comparison between experimental and numerical free surface elevation time series measured at the four wave gauges (WGi, i = 1, 2, 3, 4) used during the experiments carried out by Grilli et al. (2017). The uppermost panel refers to WG1 (i.e., the closest to the generation area), while the lowest one refers to WG4 (i.e., the farthest to the generation area), respectively. In the figure, empty black dots refer to experimental results, while thin blue lines refer to numerical ones. Furthermore, to provide a quantitative comparison between numerical and experimental results, three parameters are used: (I) the percentage difference between experimental and numerical maxima values of wave crest in the wave packet ($\Delta\eta_c^{max}$); (II) the percentage difference between experimental and numerical minima values of wave trough in the wave packet ($\Delta\eta_t^{min}$); (III) the Normalized Mean Squared Error (NMSE). These parameters, related to all the signals presented in Fig. 12, are reported in Table 2.

Overall a very good agreement between experimental and numerical results, especially referring to the first three wave crests and troughs (the most important ones), has been achieved ($0.043 \le \Delta\eta_c^{max} \le 0.309$, $0.023 \le \Delta\eta_t^{min} \le 0.045$, $0.047 \le$ NMSE ≤ 0.301). Looking at WG1 we can notice that approximately after 2 s numerical and experimental results differ slightly. In fact, small trailing waves appear not to be well reproduced by the numerical model. This is possibly related to the weak reproduction of the final part of the landslide evolution (see Fig. 8). Nevertheless, although the numerical landslide is slower than the experimental one, only in the final part, the most important part of the wave signals (first wave crests and troughs) are not much affected, indeed they are well reproduced ($\Delta\eta_t^{min}$ = 0.029 and 0.045, while NMSE, calculated without considering the trailing waves, is equal to 0.075 and 0.048 for WG1 and WG2, respectively; see Table 2). This aspect is well supported by the literature findings (Grilli et al., 2009; Clous and Abadie, 2019; Romano et al., 2020) related to tsunamis generated by submerged landslides, confirming that for submerged landslides the momentum/energy transfer between landslide and waves takes place

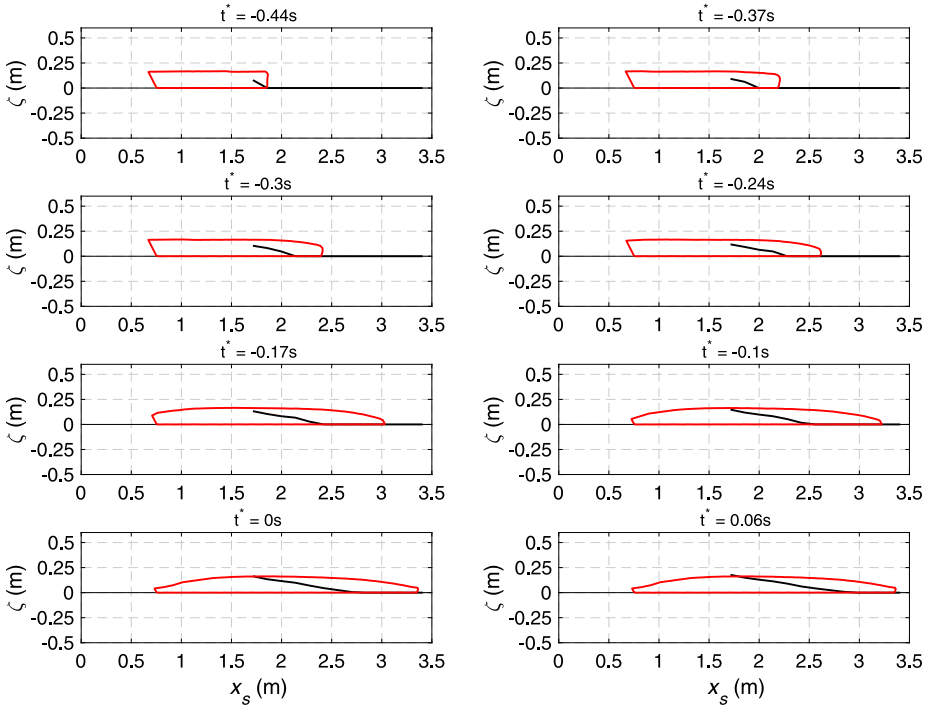

Fig. 11. Comparison between experimental (black lines) and numerical (red lines) landslide thickness ζ along the abscissa X_s after the landslide release for the 3D subaerial case of Mohammed and Fritz (2012).

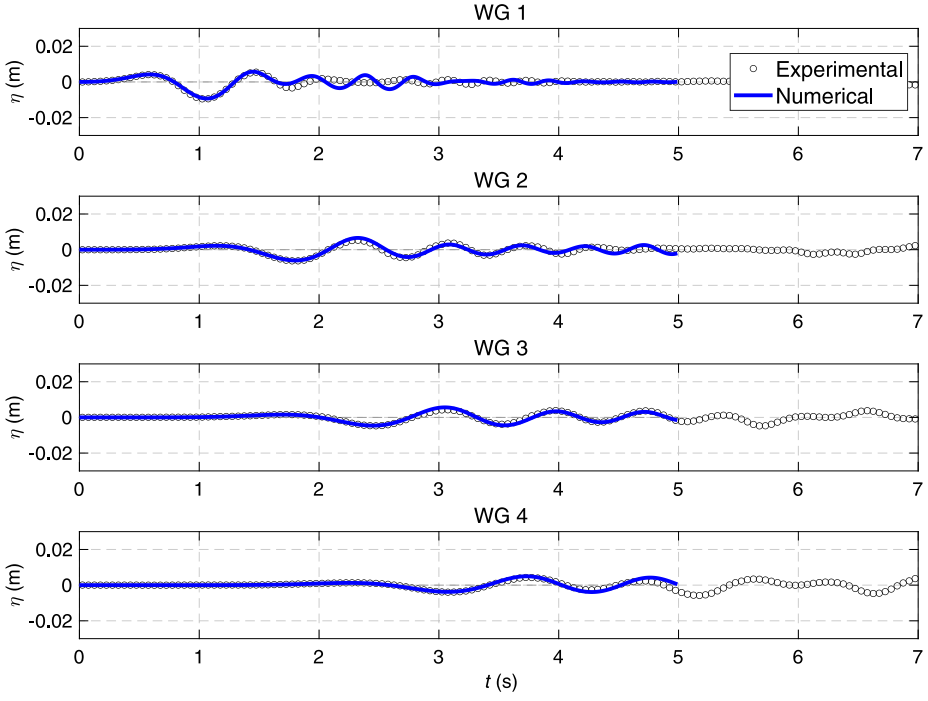

Fig. 12. Comparison between experimental and numerical free surface elevation time series measured at four wave gauges (WGi, i = 1, 2, 3, 4) for the 2D submerged case of Grilli et al. (2017).

during the very first time instants. Thus, a good modeling/reproduction of such phase results in a proper reproduction of the impulsive wave signals.

4.2.2. 2D subaerial landslide

Fig. 13 presents the comparison between experimental and numerical free surface elevation time series measured at the four wave gauges (WGi, i = 1, 2, 3, 4) used during the experiments carried out by Grilli et al. (2017). Again, the uppermost panel refers to WG1 (i.e., the closest to the generation area), while the lowest one refers to WG4 (i.e., the farthest to the generation area), respectively. In the figure, empty black dots refer to experimental results, while thin blue lines refer to numerical ones. Furthermore, for a quantitative comparison between numerical and experimental results, the same parameters previously defined ($\Delta\eta_c^{max}$, $\Delta\eta_t^{min}$ and NMSE) are used. These parameters, related to all the signals presented in Fig. 13, are reported in Table 3.

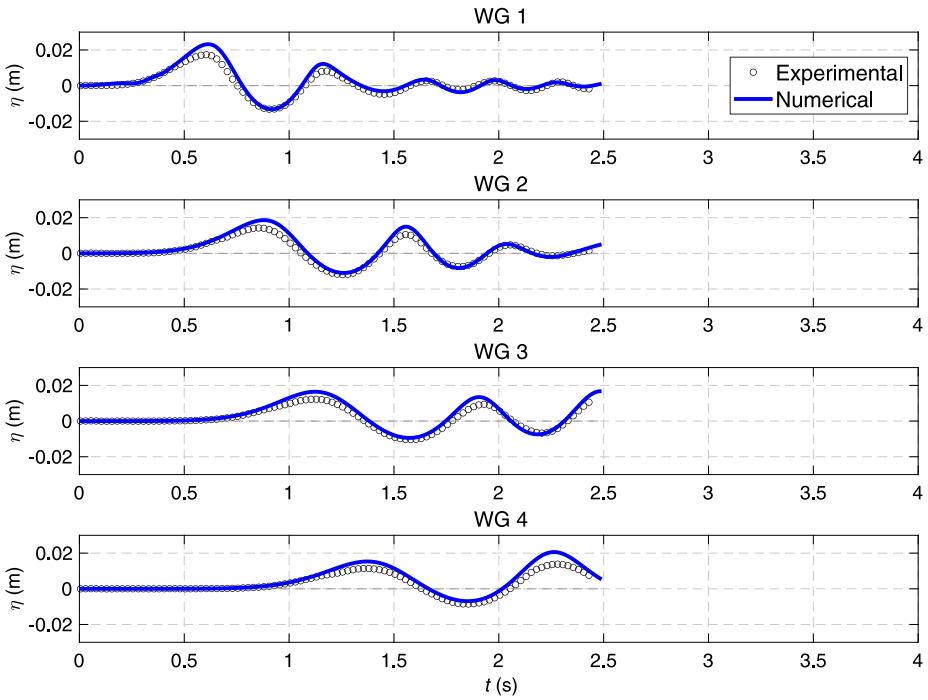

Fig. 13. Comparison between experimental and numerical free surface elevation time series measured at four wave gauges (WGi, i = 1, 2, 3, 4) for the 2D subaerial case of Viroulet et al. (2014).

Table 3
Parameter values for the quantitative comparison between numerical and experimental results of the 2D submerged case of Viroulet et al. (2014): $\Delta\eta_c^{max}$, $\Delta\eta_t^{min}$ and NMSE. Note: the values refer to the four wave gauges presented in Fig. 13.

Gauge name	$\Delta\eta_c^{max}$	$\Delta\eta_t^{min}$	NMSE
WG1	0.340	0.002	0.089
WG2	0.310	0.079	0.076
WG3	0.340	0.089	0.089
WG4	0.493	0.189	0.134

Overall a good agreement between experimental and numerical results is noticed for all the signals ($0.310 \leq \Delta\eta_c^{max} \leq 0.493$, $0.002 \leq \Delta\eta_t^{min} \leq 0.189$, $0.076 \leq \text{NMSE} \leq 0.134$). All the wave characteristics are well reproduced by the numerical model, especially referring to the first three wave crests and troughs (the most important ones in the near-field). Nevertheless, looking at all the considered wave gauges it can be seen that numerical results slightly overestimate experimental ones. This overestimation can be explained considering that the numerical approach is based on a multiphase approach, in which mixing and permeation among phases, which as pointed out by Lindstrøm (2016) and later by Heller and Ruffini (2023) are important aspects for subaerial landslide-tsunamis, are not properly modeled. Thus the lack of water permeation into the granular material may result in slightly larger wave characteristics (see Table 3).

4.2.3. Parameters uncertainty effect on free surface elevation in the near-field

As stated, this article aims at presenting and testing the numerical approach under very different landslide initial conditions. Nevertheless, it is of interest to investigate the effect of parameters uncertainty (i.e., sensitivity analysis by varying the input parameters) on the landslide and waves characteristics in the near-field. Thus, in this section a sensitivity analysis is presented to provide an estimate, although preliminary and not systematic, of the variability of the wave characteristics as far as the input rheological parameters are varied. As an example, only the friction angle is varied in a range of ±30% for both the 2D submerged and the 2D subaerial cases to preliminary investigate its influence in terms of free surface elevation in the near-field, therefore, only related to the first wave (η^{1st}) of the tsunami packet.

Fig. 14 shows the comparison, in terms of phase diagrams, between experimental (η_{exp}^{1st}, x-axis) and numerical (η_{num}^{1st}, y-axis) free surface elevation of the first wave as a function of δ at the four wave gauges for the 2D submerged case of Grilli et al. (2017). In the figure, blue dots refer to the results obtained with the reference internal friction angle, while red dots refer to those obtained by increasing this parameter by 30%. In Fig. 15 the same comparison for the 2D subaerial case of Viroulet et al. (2014) is presented. The same nomenclature of Fig. 14 is used, but in this case the internal friction angle has been decreased by 30% (red dots).

These phase diagrams show how the uncertainty on δ affects the free surface elevation in the near-field. As far as the submerged case is considered (Fig. 14), it can be seen that uncertainties in δ reflect in smaller wave troughs and crests at the four wave gauges. Wave troughs obtained by varying the mentioned parameter exhibit differences in the order of 25%, while differences are smaller if the wave crests are considered (in the order of 20%). Nevertheless, the global shape of the signals is always well reproduced.

Analogous considerations can be done for the subaerial case shown in Fig. 15, where it can be seen that uncertainties in the internal friction angle are reflected in larger wave crests and troughs at the four wave gauges. Here wave crests exhibit differences in the order of 23%, while difference are smaller if the wave troughs are considered (in the order of 15%). Also in this case, the global shape of the signals is always well reproduced.

4.2.4. 3D subaerial landslide

Conversely to the 2D cases previously discussed, in which only four wave gauges (placed along the centerline of the wave flume) were used, here, being a 3D case, much more wave gauges have been used. Moreover, also runup gauges have been deployed, as later discussed. Therefore, Fig. 16 shows the sketch of the wave and runup gauges positions used for the comparison. Wave gauges are identified by dots,

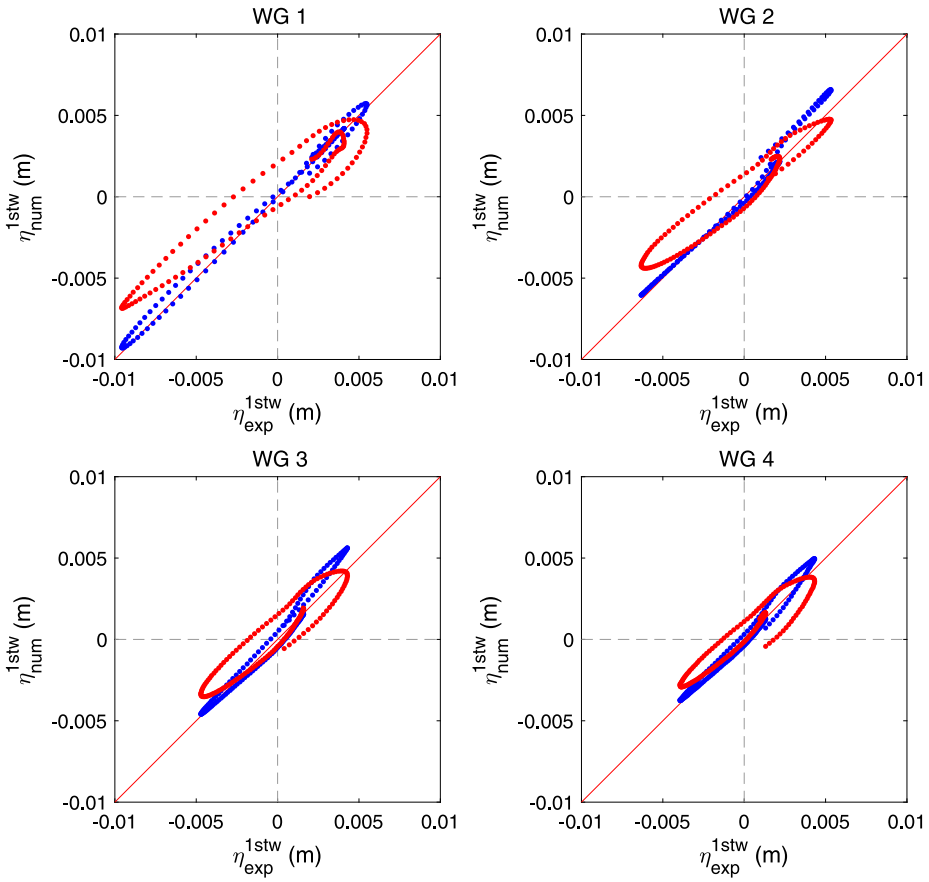

Fig. 14. Comparison between experimental (x-axis) and numerical (y-axis) free surface elevation of the first wave as a function of the friction angle at the four wave gauges for the 2D submerged case of Grilli et al. (2017). Blue dots refer to the results obtained with the reference internal friction angle, while red dots refer to those obtained by increasing this parameter by 30%.

where empty black dots refer to those wave gauges that are not used for the comparison, while full blue dots identify those that have been used for the comparison. Runup gauges are identified by red squares. Finally, the figure shows the numerical domain extension (gray filled area).

In Figs. 17 and 18 the comparison between experimental and numerical free surface elevation time series at eight selected wave gauges (WG12, WG13, WG19, WG21, WG18, WG7, WG9 and WG11, see Fig. 16) is presented. In the figures, empty black dots refer to experimental results, while thin blue lines refer to numerical ones. Fig. 17 refers to the wave gauges WG12, WG13, WG19 and WG21. Three of these wave gauges (WG12, WG13, and WG19) are placed very close to the landslide impact point, while the remaining one (WG21) is placed in a lateral position. For the quantitative comparison between numerical and experimental results, $\Delta\eta_c^{max}$, $\Delta\eta_t^{min}$ and NMSE are used. These parameters, related to all the signals presented in Figs. 17 and 18, are reported in Table 4.

Looking at Fig. 17, it can be noticed an overall very good agreement between experimental and numerical results, especially referring to the first three wave crests and troughs, while trailing waves, which are very small, are not properly reproduced ($0.029 \leq \Delta\eta_c^{max} \leq 0.374$, $0.010 \leq \Delta\eta_t^{min} \leq 0.079$, $0.097 \leq \text{NMSE} \leq 0.141$). Both wave directivity and frequency dispersion, which are extremely important for such a phenomena (Romano et al., 2016), are properly reproduced. Very similar considerations can be obtained from Fig. 18, which refers to four wave gauges placed farther than the previous one, namely: WG18 (the most lateral), WG7, WG9 and WG11. Again, an overall good agreement between experimental and numerical results is found in terms of wave characteristics, while a small delay (0.1 s) between numerical and experimental signals is noticed ($0.062 \leq \Delta\eta_c^{max} \leq 0.308$, $0.049 \leq \Delta\eta_t^{min} \leq 0.156$, $0.052 \leq \text{NMSE} \leq 0.385$).

Table 4
Parameter values for the quantitative comparison between numerical and experimental results of the 3D subaerial case of Mohammed and Fritz (2012): $\Delta\eta_c^{max}$, $\Delta\eta_t^{min}$ and NMSE. Note: the values refer to the eight wave gauges presented in Figs. 17 and 18 and to the four runup gauges presented in Fig. 16.

Gauge name	$\Delta\eta_c^{max}$	$\Delta\eta_t^{min}$	NMSE
WG12	0.083	0.063	0.097
WG13	0.029	0.056	0.127
WG19	0.101	0.010	0.126
WG21	0.374	0.079	0.141
WG18	0.308	0.049	0.052
WG7	0.062	0.156	0.344
WG9	0.182	0.142	0.385
WG11	0.086	0.049	0.281
RG1	1.318	0.131	0.347
RG2	1.327	0.318	0.344
RG3	0.850	0.266	0.265
RG4	0.417	0.128	0.207

4.3. Runup

4.3.1. 3D subaerial landslide

Finally, only for the 3D subaerial case runup time series are analyzed. In fact, as shown in Fig. 16, four runup gauges (RG1, RG2, RG3 and RG4) were placed along the planar beach that forms the experimental setup used by Mohammed and Fritz (2012). Similarly, numerical runup gauges have been placed in the numerical domain in the same positions. Fig. 19 show the comparison between experimental and numerical runup time series measured at the four runup gauges (RG1, RG2, RG3 and RG4) during the experiments. The uppermost

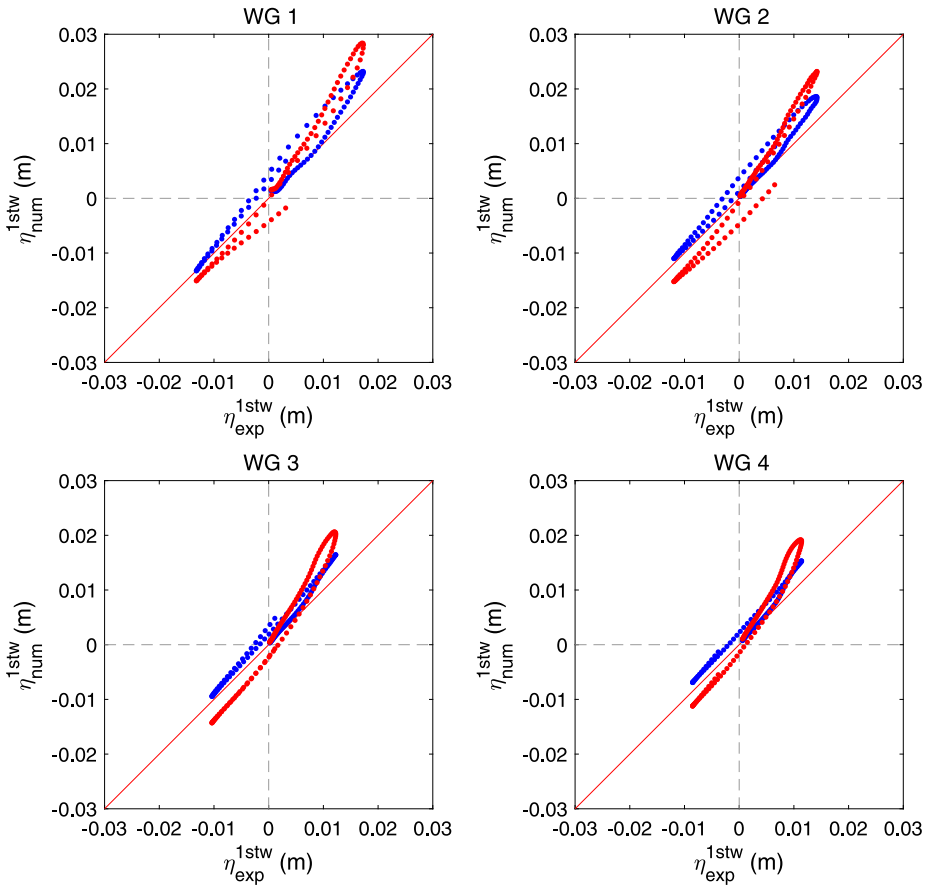

Fig. 15. Comparison between experimental (x-axis) and numerical (y-axis) free surface elevation of the first wave as a function of the friction angle at the four wave gauges for the 2D subaerial case of Viroulet et al. (2014). Blue dots refer to the results obtained with the reference internal friction angle, while red dots refer to those obtained by decreasing this parameter by 30%.

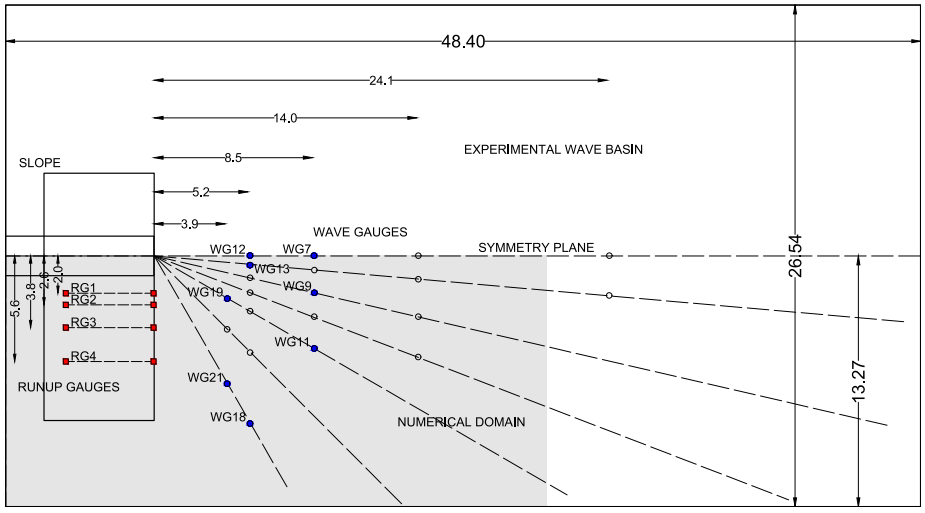

Fig. 16. Sketch of the wave and runup gauges positions used for the comparison for the 3D subaerial case of Mohammed and Fritz (2012). Note: wave gauges are identified by dots, where empty black dots refer to those wave gauges that are not used for the comparison, while full blue dots identify those that have been used for the comparison. Runup gauges are identified by red squares. The numerical domain is identified by the gray filled area. Dimensions are in meters.

panel refers to RG1 (i.e., the closest to the generation area), while the lowest one refers to RG4 (i.e., the farthest to the generation area), respectively. In the figure, empty black dots refer to experimental results, while thin blue lines refer to numerical ones. In the figure, empty black dots refer to experimental results, while thin red lines refer to numerical ones. Coherently, for the quantitative comparison between numerical and experimental runup results, $\Delta\eta_c^{max}$, $\Delta\eta_t^{min}$ and NMSE are used. These parameters, related to all the signals presented in Figs. 19, are reported in Table 4.

Fig. 19 shows that the runup pattern is well reproduced by the numerical model. Shape, timing and magnitude of runup/rundown characteristics are in line with the experimental results. The runup

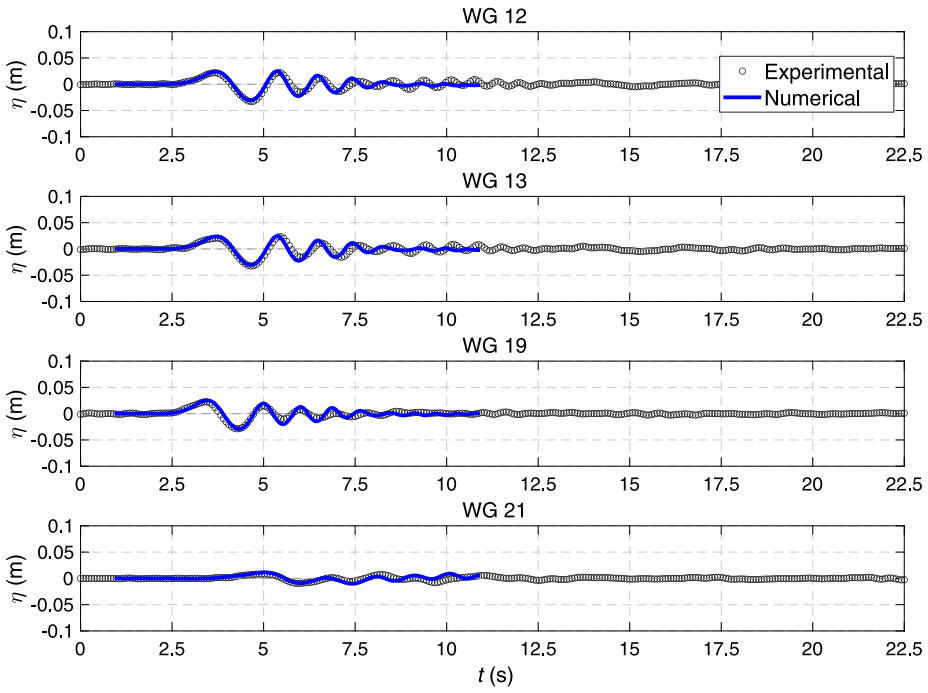

Fig. 17. Comparison between experimental and numerical free surface elevation time series measured at four wave gauges (WGi, i = 12, 13, 19, 21) for the 3D subaerial case of Mohammed and Fritz (2012).

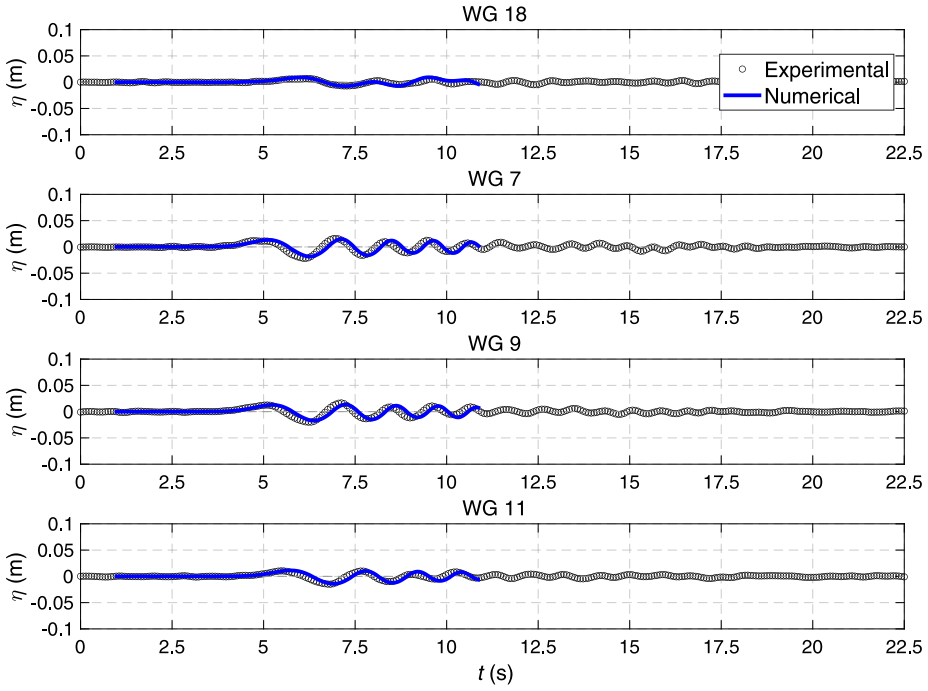

Fig. 18. Comparison between experimental and numerical free surface elevation time series measured at four wave gauges (WGi, i = 18, 7, 9, 11) for the 3D subaerial case of Mohammed and Fritz (2012).

of the first wave is significantly overestimated at the first two runup gauges ($\Delta\eta_c^{max}$ = 1.318, 1.328 for RG1 and RG2, respectively), while the rundown of the same wave, at the same gauges, as well as the global shape of the signals ($\Delta\eta_t^{min}$ = 0.131, 0.318 and NMSE = 0.347, 0.344 for RG1 and RG2, respectively), are very similar to the experimental data. This overestimation of the runup of the first wave appears to be less important as the distance from the generation area increases ($\Delta\eta_c^{max}$ = 0.850, 0.417 for RG3 and RG4, respectively). In fact, looking at RG3 and RG4 (third and fourth panel), where runup/rundown of the second and third waves are important due to frequency dispersion mechanisms and edge waves activity (Romano et al., 2013; Bellotti and Romano, 2017), runup and rundown characteristics, as well as the global shape of the signals ($\Delta\eta_t^{min}$ = 0.266, 0.128 and NMSE = 0.265, 0.207 for RG3 and RG4, respectively), are well reproduced by the numerical model. Also for the runup signals frequency dispersion mechanisms are very well reproduced by the numerical model (see third and fourth panel of Fig. 19). Trailing runup waves, which are very small, are not properly reproduced.

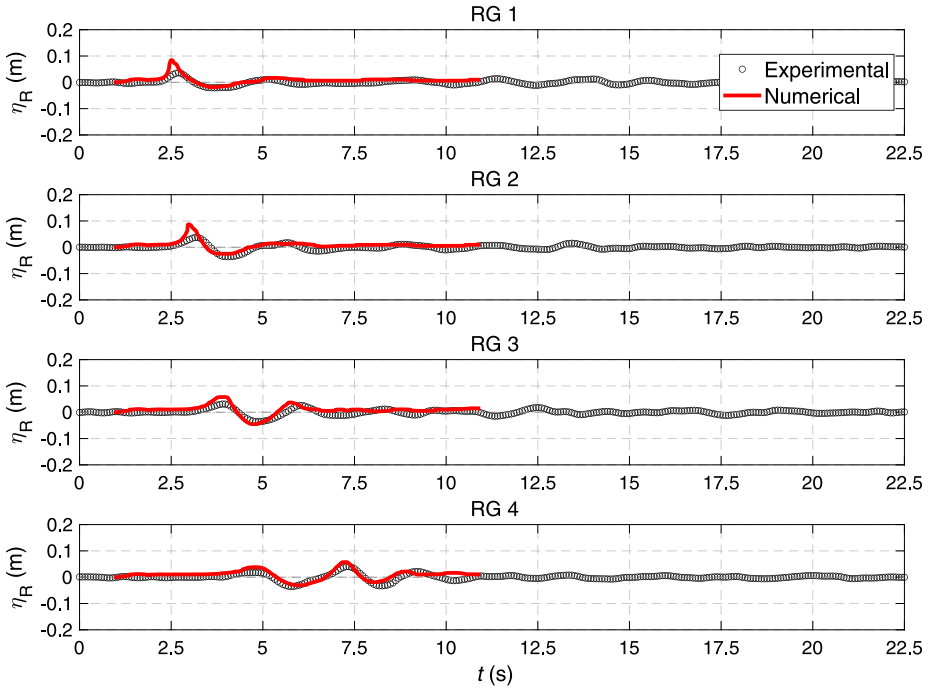

Fig. 19. Comparison between experimental and numerical runup time series measured at four runup gauges (RGi, i = 1, 2, 3, 4) for the 3D subaerial case of Mohammed and Fritz (2012).

The overestimation of the runup of the first wave close to the landslide impact point is probably due to the larger velocity of the numerical landslide, to the initial shape of the numerical granular (both initial condition effects) and to the numerical modeling of the so-called water entry problem; in fact, as previously mentioned, the present numerical approach is based on a multiphase approach, in which mixing and permeation among phases are not properly modeled. Thus, the lack of water permeation into the granular material may result in larger wave characteristics (Lindstrøm, 2016).

5. Concluding remarks

In this article, a new numerical approach to model tsunamis generated by granular landslides in OpenFOAM® is presented and validated under a wide range of geometrical configurations and landslide initial conditions. Within this numerical framework the granular material (i.e., the landslide) is modeled by using a Coulomb viscoplastic non-Newtonian rheological model (von Boetticher et al., 2016; Domnik and Pudasaini, 2012) implemented in *multiPhaseInterFoam*. The strength of this approach consists in its simplicity, flexibility and computational efficiency. In fact, only depending on few physics-based parameters it implies less uncertainty level in the parameter values determination than dense fluid models (e.g., viscosity value, Paris et al., 2021). It is a multiphase approach, therefore this implies that the modeling of the landslide dynamics could be less accurate if compared with a Euler–Euler approach (Lee and Huang, 2022; Rauter et al., 2022), as some physical phenomena (e.g., mixing and permeation among phases) are not well reproduced and/or neglected. Nevertheless, it is more computationally efficient and, at the same time, the modeling of the energy transfer between landslide and waves is very accurate, for both 2D (submerged and subaerial) as well as 3D landslides. Furthermore, the flexibility and computational efficiency favor its application to complex 3D cases, in which runup features and wave trapping phenomena are relevant aspects.

To test the numerical approach under very different initial conditions/configurations, three literature benchmark cases, identified by tsunamis experts, have been reproduced, namely: a 2D submerged landslide (Grilli et al., 2017), a 2D subaerial landslide (Viroulet et al., 2014) and 3D subaerial (accelerated) landslide (Mohammed and Fritz, 2012). Qualitative and quantitative comparison have been performed looking at landslide evolution, free surface elevation and runup (only for the 3D case) time series. For the three benchmark cases, comparing numerical and experimental results, a good agreement is found for granular material behavior (i.e., landslide evolution), while an overall very good (excellent in some cases) agreement is found as far as fluid behavior and waves characteristics (i.e., free surface elevation and runup time series) are concerned, testifying that the momentum transfer between granular and fluid phases is well reproduced by this simple rheological model. For the 2D submerged cases differences in the landslide evolution of the last time instants of the landslide are noticed, as reported also in previous works dealing with similar modeling approaches (Clous and Abadie, 2019; Paris et al., 2021). Nevertheless, as the first time instants of the landslide motion (i.e., the important ones for momentum transfer between landslide and waves) are well reproduced, this aspect does not affect the proper modeling of the wave signals. Also for the 3D subaerial case a not perfect reproduction of landslide evolution is found, probably due to the differences initial conditions used for numerical simulations. Numerical free surface elevation time series present always a very good agreement with experimental data.

Moreover, runup and rundown (for the 3D case only) are well reproduced by the numerical model in terms of shape, timing, magnitude of runup/rundown characteristics (apart from the runup of the first wave close to the landslide impact point, which are overestimated, probably due to initial conditions and numerical approximations) and physical features of the runup pattern (i.e., frequency dispersion mechanisms and edge waves activity).

Finally, it is worth to highlight that, using the numerical approach presented and validated in this article, further research is ongoing to investigate a wide range of complex physical processes/mechanisms related to landslide-generated tsunamis (e.g., wave runup pattern as a function of landslide characteristics and shoreline configurations, energy transfer, near- and far-field wave propagation and interaction with the coast, etc.), which are crucial for improving the understanding and modeling of such phenomena, especially in the near-field.

CRediT authorship contribution statement

Alessandro Romano: Conceptualization, Methodology, Investigation, Data curation, Formal analysis, Writing – original draft, Writing – review & editing, Software, Visualisation, Funding acquisition. **Javier L. Lara:** Conceptualization, Methodology, Investigation, Writing – review & editing, Funding acquisition. **Gabriel Barajas:** Conceptualization, Methodology, Investigation, Data curation, Writing – review & editing, Software, Visualisation, Funding acquisition. **Íñigo J. Losada:** Conceptualization, Methodology, Supervision, Writing – review & editing.

Declaration of competing interest

The authors declare that they have no known competing financial interests or personal relationships that could have appeared to influence the work reported in this paper.

Data availability

Data will be made available on request.

Acknowledgments

The authors acknowledge the financial support from the Government of Cantabria through the Fénix Program. The kind help of Prof. Hermann Fritz, who provided further information on the 3D subaerial case, is warmly acknowledged. A special acknowledgment is due to Prof. Bellotti for the constant support and fruitful discussions.

References

Abadie, S., Harris, J., Grilli, S., Fabre, R., 2012. Numerical modeling of Tsunami waves generated by the flank collapse of the Cumbre Vieja Volcano (La Palma, Canary Islands): Tsunami source and near field effects. J. Geophys. Res.: Oceans 117.

Abadie, S., Morichon, D., Grilli, S., Glockner, S., 2010. Numerical simulation of waves generated by landslides using a multiple-fluid Navier–Stokes model. Coast. Eng. 57, 779–794.

Abadie, S., Paris, A., Ata, R., Le Roy, S., Arnaud, G., Poupardin, A., Clous, L., Heinrich, P., Harris, J., Pedreros, R., et al., 2019. La Palma landslide Tsunami: computation of the Tsunami source with a calibrated multi-fluid Navier–Stokes model and wave impact assessment with propagation models of different types. Natural Hazards Earth Syst. Sci. Discuss. 1–50.

Ancey, C., 2007. Plasticity and geophysical flows: A review. J. Non-Newtonian Fluid Mech. 142, 4–35.

Bellotti, G., Cecioni, C., De Girolamo, P., 2008. Simulation of small-amplitude frequency-dispersive transient waves by means of the mild-slope equation. Coast. Eng. 55, 447–458.

Bellotti, G., Romano, A., 2017. Wavenumber-frequency analysis of landslide-generated Tsunamis at a conical island. Part II: EOF and modal analysis. Coast. Eng. 128, 84–91.

Brackbill, J.U., Kothe, D.B., Zemach, C., 1992. A continuum method for modeling surface tension. J. Comput. Phys. 100, 335–354.

Cecioni, C., Romano, A., Bellotti, G., Di Risio, M., De Girolamo, P., 2011. Real-time inversion of Tsunamis generated by landslides. Natural Hazards Earth Syst. Sci. 11, 2511–2520.

Chen, F., Heller, V., Briganti, R., 2020. Numerical modelling of Tsunamis generated by iceberg calving validated with large-scale laboratory experiments. Adv. Water Resour. 142, 103647.

Clous, L., Abadie, S., 2019. Simulation of energy transfers in waves generated by granular slides. Landslides 1–17.

De Girolamo, P., Di Risio, M., Romano, A., Molfetta, M., 2014. Landslide Tsunami: physical modeling for the implementation of Tsunami early warning systems in the Mediterranean Sea. Procedia Eng. 70, 429–438.

Di Risio, M., Bellotti, G., Panizzo, A., De Girolamo, P., 2009a. Three-dimensional experiments on landslide generated waves at a sloping coast. Coast. Eng. 56, 659–671.

Di Risio, M., De Girolamo, P., Bellotti, G., Panizzo, A., Aristodemo, F., Molfetta, M.G., Petrillo, A.F., 2009b. Landslide-generated Tsunamis runup at the coast of a conical island: New physical model experiments. J. Geophys. Res.-Oceans 114.

Domnik, B., Pudasaini, S.P., 2012. Full two-dimensional rapid chute flows of simple viscoplastic granular materials with a pressure-dependent dynamic slip-velocity and their numerical simulations. J. Non-Newton. Fluid Mech. 173, 72–86.

Domnik, B., Pudasaini, S.P., Katzenbach, R., Miller, S.A., 2013. Coupling of full two-dimensional and depth-averaged models for granular flows. J. Non-Newton. Fluid Mech. 201, 56–68.

Enet, F., Grilli, S.T., 2007. Experimental study of Tsunami generation by three-dimensional rigid underwater landslides. J. Waterw. Port Coast. Ocean Eng.-ASCE 133, 442–454.

Franci, A., Cremonesi, M., Perego, U., Crosta, G., Oñate, E., 2020. 3D simulation of Vajont disaster. Part 1: Numerical formulation and validation. Eng. Geol. 279, 105854.

Fritz, H.M., Mohammed, F., Yoo, J., 2009. Lituya Bay landslide impact generated mega-tsunami 50th anniversary. Pure Appl. Geophys. 166, 153–175.

Grilli, S.T., Shelby, M., Kimmoun, O., Dupont, G., Nicolsky, D., Ma, G., Kirby, J.T., Shi, F., 2017. Modeling coastal Tsunami hazard from submarine mass failures: effect of slide rheology, experimental validation, and case studies off the US east coast. Natural Hazards 86, 353–391.

Grilli, S.T., Tappin, D.R., Carey, S., Watt, S.F., Ward, S.N., Grilli, A.R., Engwell, S.L., Zhang, C., Kirby, J.T., Schambach, L., et al., 2019. Modelling of the Tsunami from the December 22, 2018 lateral collapse of Anak Krakatau volcano in the Sunda Straits, Indonesia. Sci. Rep. 9, 11946.

Grilli, S.T., Taylor, O.D.S., Baxter, C.D., Maretzki, S., 2009. A probabilistic approach for determining submarine landslide Tsunami hazard along the upper East Coast of the United States. Mar. Geol. 264, 74–97.

Guan, X., Shi, H., 2023. Translational momentum of deformable submarine landslides off a slope. J. Fluid Mech. 960 (A23).

Heidarzadeh, M., Ishibe, T., Sandanbata, O., Muhari, A., Wijanarto, A.B., 2020. Numerical modeling of the subaerial landslide source of the 22 December 2018 Anak Krakatoa volcanic Tsunami, Indonesia. Ocean Eng. 195, 106733.

Heller, V., Bruggemann, M., Spinneken, J., Rogers, B.D., 2016. Composite modelling of subaerial landslide–tsunamis in different water body geometries and novel insight into slide and wave kinematics. Coast. Eng. 109, 20–41.

Heller, V., Hager, W.H., 2010. Impulse product parameter in landslide generated impulse waves. J. Waterw. Port Coast. Ocean Eng. 136, 145–155.

Heller, V., Ruffini, G., 2023. A critical review about generic subaerial landslide-tsunami experiments and options for a needed step change. Earth-Sci. Rev. 104459.

Heller, V., Spinneken, J., 2013. Improved landslide-tsunami prediction: effects of block model parameters and slide model. J. Geophys. Res.: Oceans 118, 1489–1507.

Heller, V., Spinneken, J., 2015. On the effect of the water body geometry on landslide–tsunamis: physical insight from laboratory tests and 2D to 3D wave parameter transformation. Coast. Eng. 104, 113–134.

Higuera, P., Lara, J.L., Losada, I.J., 2013a. Realistic wave generation and active wave absorption for Navier–Stokes models: Application to OpenFOAM®. Coast. Eng. 71, 102–118.

Higuera, P., Lara, J.L., Losada, I.J., 2013b. Simulating coastal engineering processes with OpenFOAM®. Coast. Eng. 71, 119–134.

Jasak, H., 1996. Error Analysis and Estimation for the Finite Volume Method with Applications to Fluid Flows (Ph.D. thesis). Imperial College London (University of London).

Kim, G.B., Cheng, W., Sunny, R.C., Horrillo, J.J., McFall, B.C., Mohammed, F., Fritz, H.M., Beget, J., Kowalik, Z., 2019a. Three dimensional landslide generated Tsunamis: Numerical and physical model comparisons. Landslides 17, 1–17.

Kim, J., Løvholt, F., Issler, D., Forsberg, C.F., 2019b. Landslide material control on Tsunami genesis: the storegga slide and Tsunami (8, 100 years bp). J. Geophys. Res.: Oceans 124, 3607–3627.

Kirby, J.T., Grilli, S.T., Horrillo, J., Liu, P.L.F., Nicolsky, D., Abadie, S., Ataie-Ashtiani, B., Castro, M.J., Clous, L., Escalante, C., et al., 2022. Validation and inter-comparison of models for landslide Tsunami generation. Ocean Model. 170, 101943.

Larsen, B.E., Fuhrman, D.R., 2018. On the over-production of turbulence beneath surface waves in Reynolds-Averaged Navier–Stokes models. J. Fluid Mech. 853, 419–460.

Lee, C.H., Huang, Z., 2022. Effects of grain size on subaerial granular landslides and resulting impulse waves: experiment and multi-phase flow simulation. Landslides 19, 137–153.

Lindstrøm, E.K., 2016. Waves generated by subaerial slides with various porosities. Coast. Eng. 116, 170–179.

Liu, P.F., Wu, T.R., Raichlen, F., Synolakis, C., Borrero, J., 2005. Runup and rundown generated by three-dimensional sliding masses. J. Fluid Mech. 536, 107–144.

Løvholt, F., Harbitz, C.B., Haugen, K.B., 2005. A parametric study of Tsunamis generated by submarine slides in the Ormen Lange/Storegga area off western Norway. In: Ormen Lange–An Integrated Study for Safe Field Development in the Storegga Submarine Area. Elsevier, pp. 219–231.

Løvholt, S., Harbitz, C.B., 2020. On the landslide Tsunami uncertainty and hazard. Landslides 17, 2301–2315.

Lynett, P., Liu, P.L.F., 2005. A numerical study of the run-up generated by three-dimensional landslides. J. Geophys. Res.: Oceans 110.

Ma, G., Kirby, J.T., Hsu, T.J., Shi, F., 2015. A two-layer granular landslide model for Tsunami wave generation: theory and computation. Ocean Model. 93, 40–55.

Marschall, H., Hinterberger, K., Schüler, C., Habla, F., Hinrichsen, O., 2012. Numerical simulation of species transfer across fluid interfaces in free-surface flows using OpenFOAM. Chem. Eng. Sci. 78, 111–127.

McFall, B.C., Fritz, H.M., 2016. Physical modelling of Tsunamis generated by three-dimensional deformable granular landslides on planar and conical island slopes. Proc. R. Soc. Lond. Ser. A Math. Phys. Eng. Sci. 472 (2188), 20160052.

Miller, G.S., Take, W.A., Mulligan, R.P., McDougall, S., 2017. Tsunamis generated by long and thin granular landslides in a large flume. J. Geophys. Res.: Oceans 122, 653–668.

Mohammed, F., Fritz, H.M., 2012. Physical modeling of Tsunamis generated by three-dimensional deformable granular landslides. J. Geophys. Res.: Oceans (1978–2012) 117.

Montagna, F., Bellotti, G., Di Risio, M., 2011. 3D numerical modeling of landslide-generated Tsunamis around a conical island. Nat. Hazards 58, 591–608.

Mulligan, R.P., Franci, A., Celigueta, M.A., Take, W.A., 2020. Simulations of landslide wave generation and propagation using the particle finite element method. J. Geophys. Res.: Oceans 125, e2019JC015873.

Panizzo, A., De Girolamo, P., Di Risio, M., Maistri, A., Petaccia, A., 2005. Great landslide events in Italian artificial reservoirs. Nat. Hazards Earth Syst. Sci. 5, 733–740.

Paris, A., Heinrich, P., Abadie, S., 2021. Landslide Tsunamis: Comparison between depth-averaged and Navier-Stokes models. Coast. Eng. 170, 104022.

Paris, A., Heinrich, P., Paris, R., Abadie, S., 2020. The December 22, 2018 Anak Krakatau, Indonesia, landslide and Tsunami: preliminary modeling results. Pure Appl. Geophys. 177, 571–590.

Rauter, M., Hoße, R., Take, W., Løvholt, F., 2021. Numerical simulation of impulse wave generation by idealized landslides with OpenFOAM. Coast. Eng. 165, 103815.

Rauter, M., Viroulet, S., Gylfadóttir, S.S., Fellin, W., Løvholt, F., 2022. Granular porous landslide Tsunami modelling–the 2014 Lake Askja flank collapse. Nature Commun. 13, 1–13.

Romano, A., Bellotti, G., Di Risio, M., 2013. Wavenumber–frequency analysis of the landslide-generated Tsunamis at a conical island. Coast. Eng. 81, 32–43.

Romano, A., Di Risio, M., Bellotti, G., Molfetta, M., Damiani, L., De Girolamo, P., 2016. Tsunamis generated by landslides at the coast of conical islands: experimental benchmark dataset for mathematical model validation. Landslides 13, 1379–1393.

Romano, A., Di Risio, M., Molfetta, M.G., Bellotti, G., Pasquali, D., Sammarco, P., Damiani, L., De Girolamo, P., 2017. 3D physical modeling of Tsunamis generated by submerged landslides at a conical island: the role of initial acceleration. Coast. Eng. Proc. 1 (35), 14.

Romano, A., Lara, J.L., Barajas, G., Di Paolo, B., Bellotti, G., Di Risio, M., Losada, I.J., De Girolamo, P., 2020. Tsunamis generated by submerged landslides: numerical analysis of the near-field wave characteristics. J. Geophys. Res.: Oceans 125, e2020JC016157.

Ruffini, G., Heller, V., Briganti, R., 2019. Numerical modelling of landslide-tsunami propagation in a wide range of idealised water body geometries. Coast. Eng. 103518.

Shi, C., An, Y., Wu, Q., Liu, Q., Cao, Z., 2016. Numerical simulation of landslide-generated waves using a soil–water coupling smoothed particle hydrodynamics model. Adv. Water Resour. 92, 130–141.

Si, P., Shi, H., Yu, X., 2018. A general numerical model for surface waves generated by granular material intruding into a water body. Coast. Eng. 142, 42–51.

Synolakis, C.E., Bardet, J.P., Borrero, J.C., Davies, H.L., Okal, E.A., Silver, E.A., Sweet, S., Tappin, D.R., 2002. The slump origin of the 1998 Papua New Guinea Tsunami. Proc. R. Soc. Lond. Ser. A Math. Phys. Eng. Sci. 458, 763–789.

Takabatake, T., Han, D.C., Valdez, J.J., Inagaki, N., Mäll, M., Esteban, M., Shibayama, T., 2022. Three-dimensional physical modeling of Tsunamis generated by partially submerged landslides. J. Geophys. Res.: Oceans 127, e2021JC017826.

Tinti, S., Manucci, A., Pagnoni, G., Armigliato, A., Zaniboni, F., 2005. The 30 December 2002 landslide-induced Tsunamis in Stromboli: sequence of the events reconstructed from the eyewitness accounts. Nat. Hazards Earth Syst. Sci. 5, 763–775.

Viroulet, S., Sauret, A., Kimmoun, O., 2014. Tsunami generated by a granular collapse down a rough inclined plane. Europhys. Lett. 105 (34004).

von Boetticher, A., Turowski, J.M., McArdell, B.W., Rickenmann, D., Kirchner, J.W., 2016. Debrisintermixing-2.3: A finite volume solver for three-dimensional debris-flow simulations with two calibration parameters–Part 1: Model description. Geosci. Model Dev. 9, 2909–2923.

Watts, P., 1998. Wavemaker curves for Tsunamis generated by underwater landslides. J. Waterw. Port Coast. Ocean Eng. 124, 127–137.

Watts, P., Grilli, S., Kirby, J., Fryer, G., Tappin, D., 2003. Landslide Tsunami case studies using a Boussinesq model and a fully nonlinear Tsunami generation model. Nat. Hazards Earth Syst. Sci. 3, 391–402.

Weller, H.G., 2008. A New Approach to VOF-Based Interface Capturing Methods for Incompressible and Compressible Flow. Report TR/HGW 4, OpenCFD Ltd..

Whittaker, C., Nokes, R., Lo, H.Y., Liu, P.F., Davidson, M., 2017. Physical and numerical modelling of Tsunami generation by a moving obstacle at the bottom boundary. Environ. Fluid Mech. 17, 929–958.

Yavari-Ramshe, S., Ataie-Ashtiani, B., 2016. Numerical modeling of subaerial and submarine landslide-generated Tsunami waves: recent advances and future challenges. Landslides 13, 1325–1368.

Zengaffinen, T., Løvholt, F., Pedersen, G.K., Harbitz, C.B., 2020. Effects of rotational submarine slump dynamics on Tsunami genesis: new insight from idealized models and the 1929 Grand Banks event. Geol. Soc., London, Special Publ. 500, 41–61.

Zitti, G., Ancey, C., Postacchini, M., Brocchini, M., 2016. Impulse waves generated by snow avalanches: momentum and energy transfer to a water body. J. Geophys. Res.: Earth Surf. 121, 2399–2423.